

# Materials design of dynamically stable $d^9$ layered nickelates

Motoaki Hirayama,<sup>1,\*</sup> Terumasa Tadano,<sup>2,†</sup> Yusuke Nomura,<sup>1</sup> and Ryotaro Arita<sup>1,3</sup>

<sup>1</sup>*RIKEN Center for Emergent Matter Science, 2-1 Hirosawa, Wako, Saitama 351-0198, Japan*

<sup>2</sup>*Research Center for Magnetic and Spintronic Materials,*

*National Institute for Materials Science, Tsukuba 305-0047, Japan*

<sup>3</sup>*Department of Applied Physics, The University of Tokyo, 7-3-1 Hongo, Bunkyo-ku, Tokyo 113-8656*

(Dated: December 21, 2024)

Motivated by the recent discovery of superconductivity in the Sr-doped layered nickelate NdNiO<sub>2</sub>, we perform a systematic computational materials design of layered nickelates that are dynamically stable and whose electronic structure better mimics the electronic structure of high- $T_c$  cuprates than NdNiO<sub>2</sub>. While the Ni 3d orbitals are self-doped from the  $d^9$  configuration in NdNiO<sub>2</sub> and the Nd-layer states form Fermi pockets, we find more than 10 promising compounds for which the self-doping is almost or even completely suppressed. We derive effective single-band models for those materials and find that they are in the strongly-correlated regime. We also investigate the possibility of palladate analogues of high- $T_c$  cuprates. Once synthesized, these nickelates and palladates will provide a firm ground for studying superconductivity in the Mott-Hubbard regime of the Zaanen-Sawatzky-Allen classification.

## I. INTRODUCTION

The recent discovery of superconductivity in the Sr-doped nickelate NdNiO<sub>2</sub> [1] offers a new exciting platform for investigating unconventional superconductivity in layered correlated materials, thus prompting active theoretical and experimental studies [2–16]. Here, one fascinating avenue to explore is computational materials design of new nickelate superconductors exploiting the layered crystal structure. Since NdNiO<sub>2</sub> has alternate stacks of the superconducting NiO<sub>2</sub> layer and the Nd layer, we can design different nickelate superconductors by replacing the Nd layer. Indeed, for layered superconductors such as high transition-temperature ( $T_c$ ) cuprates [17], iron-based superconductors [18], BiS<sub>2</sub> superconductors [19], a rich variety of families exhibiting different physical properties have been discovered. While superconductivity has been observed only in Sr-doped NdNiO<sub>2</sub> so far, discovery of other nickelate superconductors would have a great impact on the studies not only of nickelates but also of other layered transition-metal oxides.

Although the low-energy electronic structure of NdNiO<sub>2</sub> is quite similar to that of high- $T_c$  cuprates, there is a distinct difference; extra states cross the Fermi level and induces the self-doping of the Ni 3d <sub>$x^2-y^2$</sub>  orbital [2, 8, 12, 20]. In particular, the Fermi pocket around the A point in the Brillouin zone is noticeable which is formed by the bonding orbital between the interstitial  $s$  state formed in the Nd layer and the Nd 5d <sub>$xy$</sub>  state (see Fig. 1). We have recently shown that the size of the extra Fermi pocket can be reduced by changing the Nd layer with other anion layers [8]. This finding motivated us to seek even better compositions and structures that do not

form Fermi pockets and make the valence of Ni almost or even exactly +1.

In this paper, we present a systematic computational search for new layered nickelates that are dynamically stable and whose electronic structure well mimics that of high- $T_c$  cuprates. When designing possible new structures of layered nickelates in a controlled and systematic way, we refer to the seminal work by Tokura and Arima in 1990 for high- $T_c$  cuprates [21]. There, they introduced the concept of “block layer” (BL), which is an atomic layer composed of metallic ions and oxygens or halogens, for classifying and designing the crystal structures of high- $T_c$  cuprates. Among the 14 BLs they proposed, 10 BLs contain apical oxygen, which is harmful to realizing the valence of Ni<sup>1+</sup> (or equivalently  $d^9$  configuration). Therefore, we focus on the other four BLs, which are free from apical oxygens, as a building block of nickelates. The constituent elements of the four BLs are also generated systematically by considering the requirements of the valence of a BL.

Based on our design principle, we systematically generate 57 new layered nickelates. To make our computational prediction more reliable, we assess the dynamical stability of these nickelates by performing comprehensive phonon calculations and show that 16 nickelates are indeed dynamically stable. For the selected dynamically stable systems, we further derive effective single-band Hamiltonians and compare them with that for NdNiO<sub>2</sub>. We show that all of the newly proposed nickelates reside in the strongly correlated regime without forming an extra Fermi pocket as large as that of NdNiO<sub>2</sub>. Indeed, some nickelates have no extra Fermi pocket other than the Ni 3d <sub>$x^2-y^2$</sub>  band and better mimic the band structure of high- $T_c$  cuprates. In such nickelates, a single-band Hubbard model will give a good description because the Ni 3d <sub>$x^2-y^2$</sub>  band is well isolated from the other 3d bands, and the charge transfer energy is large. Therefore, they provide, once synthesized, a better platform for studying superconductivity in the Mott-Hubbard regime, which

\* motoaki.hirayama@riken.jp

† TADANO.Terumasa@nims.go.jp

will also help the understanding of the superconductivity in high- $T_c$  cuprates realized in the charge-transfer regime.

The structure of the paper is as follows. After briefly discussing the origin of the extra Fermi pocket observed in NdNiO<sub>2</sub> in Sec. II, we describe our detailed strategy for the materials design in Secs. III and IV. In Sec. V, we identify the dynamically stable materials by performing *ab initio* phonon calculations. We then present the electronic structure of the stable materials in Sec. VI and derive effective single-band models in Sec. VII. In Sec. VIII, we further extend our systematic search to Pd oxides (palladates). Sec. IX is devoted to the summary of the present study.

## II. ORIGIN OF EXTRA FERMI POCKET IN NdNiO<sub>2</sub>

We first discuss the origin of the large extra Fermi pocket in the low-energy electronic structure of NdNiO<sub>2</sub>. Figure 1(a) shows the calculated electronic band structure of NdNiO<sub>2</sub>. While the electronic structure of NdNiO<sub>2</sub> looks very similar to that of high- $T_c$  cuprates in that the Ni  $3d_{x^2-y^2}$  orbital makes a large two-dimensional Fermi surface, one notable difference exists: the presence of extra states intersecting the Fermi level. In particular, the extra Fermi pocket around the A point of the Brillouin zone is noteworthy, which is formed by the bonding state between the interstitial  $s$ -like orbital and the Nd  $5d_{xy}$  orbital shown respectively in Figs. 1(d) and 1(e). The hybridization between the bonding state and the Ni  $3d_{x^2-y^2}$  orbital is small [8], but the formation of the extra Fermi pocket induces the self-doping of the Ni  $3d_{x^2-y^2}$  orbital [2, 8, 12, 20].

The presence of the extra Fermi pocket can mainly be attributed to the relatively high energy level of the Ni  $3d_{x^2-y^2}$  orbital of the NiO<sub>2</sub> layer compared with that of the Cu  $3d_{x^2-y^2}$  orbital in a CuO<sub>2</sub> layer. To realize the  $d^9$  electron configuration in a NiO<sub>2</sub> or CuO<sub>2</sub> plane, the valence of Ni and Cu must be +1 and +2, respectively. Since the most common oxidation state of these transition metals is +2, (NiO<sub>2</sub>)<sup>3-</sup> is energetically less stable than (CuO<sub>2</sub>)<sup>2-</sup>, making the energy level of the Ni  $3d_{x^2-y^2}$  orbital higher than that of the Cu  $3d_{x^2-y^2}$  orbital.

Since it is difficult to control the energy level of the Ni  $3d_{x^2-y^2}$  orbital, our strategy here is to lift the energy level of the bonding orbital around the A point and thereby remove the extra Fermi pocket. The energy level of the bonding orbital will be lifted by

- raising the energy level of the interstitial  $s$  and the cation  $d_{xy}$  orbitals.
- reducing the band splitting between the bonding and antibonding orbitals.

It can be achieved by replacing the Nd layer with other layers, which affects both of the above two factors [8].

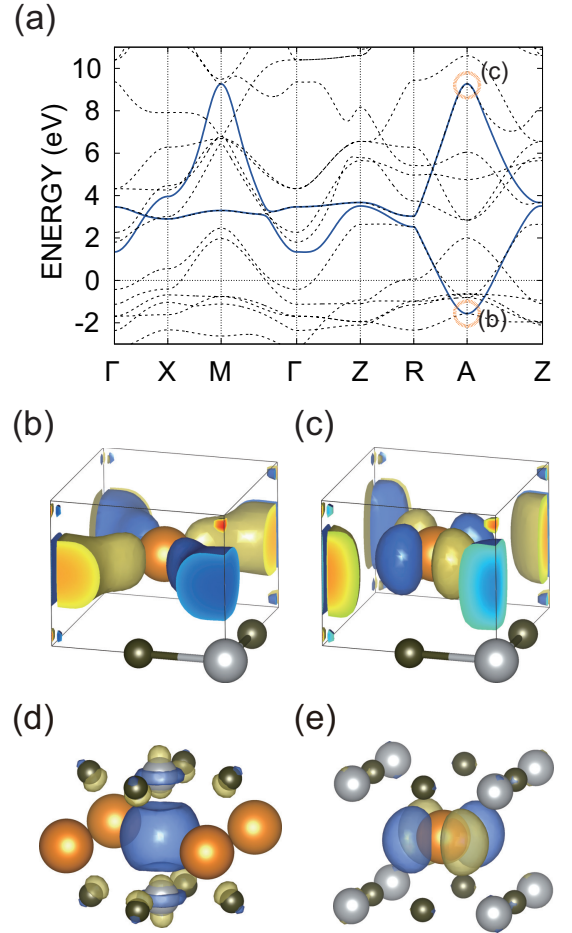


FIG. 1. (a) Electronic band structure of NdNiO<sub>2</sub> (black dotted line) and that of a two-orbital tight-binding model for the interstitial  $s$  and Nd  $5d_{xy}$  Wannier orbitals (blue solid line). The energy is measured from the Fermi level. (b),(c) Bloch function of the band bottom of the bonding band between the interstitial  $s$  orbital and the Nd  $5d_{xy}$  orbital and the band top of the antibonding band at the A point, respectively. The results shown in (b) and (c) correspond to the states indicated by the orange open circles in (a). (d),(e) Wannier function of the interstitial  $s$  orbital and the Nd  $5d_{xy}$  orbital, respectively. The calculation is performed by using OpenMX [22] (see Appendix A for the computational details).

## III. CHOICE OF BLOCK LAYERS

In this section, we discuss how we generate new layered nickelate structures that can potentially realize an ideal  $d^9$  configuration where only the Ni  $3d_{x^2-y^2}$  band forms the Fermi surface. To achieve the structure generation in a systematic and controlled way, we refer to the work of Tokura and Arima for high  $T_c$  cuprates [21], where they introduced the concept of “Block Layer” (BL) for classifying and designing crystal structures of cuprates. According to their classification, there are 14 types of BLs. Among them, 10 types of BLs contain apical oxy-

gen. However, the valence of Ni cannot be monovalent when it is surrounded by six oxygen atoms. Therefore, we hereafter consider the other 4 BLs that are free from apical oxygen and use their appropriate variants as a building block of new layered nickelates. The considered BLs are the V-, G-,  $H_1$ - and  $H_2$ -type BLs in Ref. 21, whose crystal structures are shown in Fig. 2. Here, the gray and black spheres in the rectangular box represent cations and anions, respectively (see Table I for the choice of cation and anion elements). The top and bottom planes correspond to the  $NiO_2$  sheet. While the position of Ni is the same for the top and the bottom for the V and  $H_1$  blocks (Figs. 2(a) and (b), see also Figs. 3(a),(b) and (c)), there is a “phase shift” for the G and  $H_2$  blocks (Figs. 2(c) and (d), see also Figs. 3(d),(e) and (f)).

To realize an ideal  $d^9$  configuration of Ni, we need to prevent the BL band from making the Fermi surface. Since the energy level of the Ni  $3d_{x^2-y^2}$  orbital is close to the conduction band, the cation elements in the BL should be chosen carefully so that the energy level of the BL band becomes sufficiently high. Therefore, for the cations in BLs, we use elements in the 1–3 groups (such as Sr and La), which strongly favors closed shell. This is in stark contrast with the case of the high- $T_c$  cuprates, where elements in the 11–13 groups (such as Hg and Tl) can be used as cations in the BLs thanks to the larger work function of  $Cu^{2+}$ .

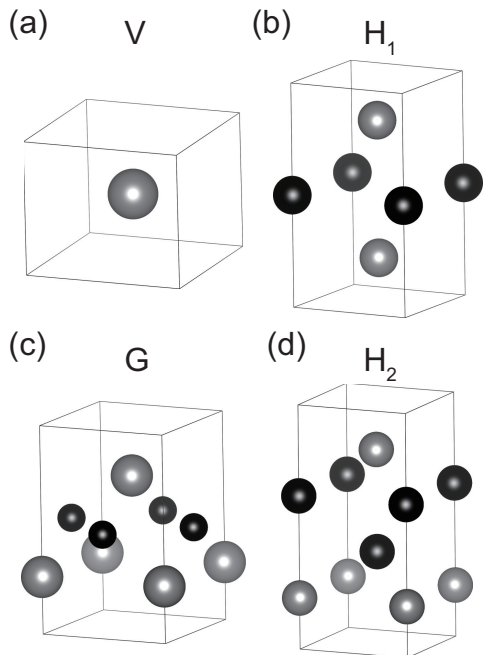


FIG. 2. Crystal structure of the block layer: (a) V-block, (b)  $H_1$ -block, (c) G-block, and (d)  $H_2$ -block.

#### IV. CRYSTAL STRUCTURE OF CANDIDATE MATERIALS

Let us now assemble the  $NiO_2$  layer and the BLs considered in the previous section. As is listed in Table I, there are five possible families. For the V-type BL in high- $T_c$  cuprates, divalent cations such as  $Ca^{2+}$  have been considered. In the case of nickelates, the cation should be trivalent to make the valence of the  $NiO_2$  layer be 3–. Indeed, the 112 family, which has already been synthesized experimentally [23–26], contains a V-type BL consisting of  $La^{3+}$  or  $Nd^{3+}$ . Since the work function of these elements is not sufficiently small, the  $NiO_2$  layer in the 112 family is self-doped and electrons in the BL form Fermi pockets around the  $\Gamma$  and A points.

Regarding the  $H_1$ -type BL in high- $T_c$  cuprates, a halogen layer sandwiched by two layers of divalent cations such as  $Sr^{2+}$  and  $Ba^{2+}$  has been considered. However, the formation of a stable square  $CuO_2$  plane has not been reported for the  $H_1$ -type BLs, with which lower-symmetry structures are favored [27]. Here, to improve the stability of layered nickelates with the  $H_1$ -type BLs, we consider two variants of the original  $H_1$  structure. In  $AB_2NiO_4$  (1214 family, Fig. 3(b)), we replace the divalent cation with a trivalent cation  $B$ , and the halogen layer is replaced with an  $(AO_2)^{3-}$  layer with  $A$  being a monovalent cation. In  $AB_2NiO_3$  (1213 family, Fig. 3(c)), we consider divalent cation  $B$ , and the halogen layer is replaced with an  $(AO)^-$  layer.

The G-type block can be seen in the mother compound of the  $n$ -type cuprate superconductor with the T'-structure [28]. The multilayer nickelates  $Nd_4Ni_3O_8$  [29–31] and  $La_3Ni_2O_6$  [32] can be regarded as a stacked heterostructure of the V-type and G-type blocks. While the valence of the G-type block ( $Ln_2O_2$ ) is 2+, we need a BL with a valence of 3+. Thus we consider the following two variants of the G-type block. One is  $A_2B'_2$ , where  $A$  is a trivalent cation, such as Y, La, Nd, Lu, and  $B'$  is an anion with a valence of 1.5– (see Fig. 3(d)). This situation can be realized when  $B'$  is  $O_{0.5}F_{0.5}$  or  $O_{0.5}H_{0.5}$ . Another possibility is  $B' = O_{0.75}\square_{0.25}$ , i.e., the situation where 25% of the  $B'$ -sites are vacant. The other variant is  $A'_2B_2$ , where  $A'$  is a cation with a valence of 2.5+ and  $B$  is a halogen such as F, Cl, Br and I (see Fig. 3(e)). The valence of 2.5+ can be realized by mixing the divalent and trivalent cations with the ratio 1:1. Another possibility is that 5/6 of the  $A'$  sites are occupied by a 3+ cation and 1/6 are vacant. In the present study, for  $A'$ , we consider the case of  $Ba_{0.5}La_{0.5}$ .

Finally, let us consider the possibility of the  $H_2$ -type family. Again, while the  $H_2$ -type BL in high- $T_c$  cuprate is divalent, we need a trivalent BL for nickelates. Figure 3(f) shows the crystal structure of  $A'_2NiO_2B_2$ , where  $A'$  is a cation with a valence of 2.5+. As in the case of the G-family, we consider  $Ba_{0.5}La_{0.5}$  as  $A'$ .

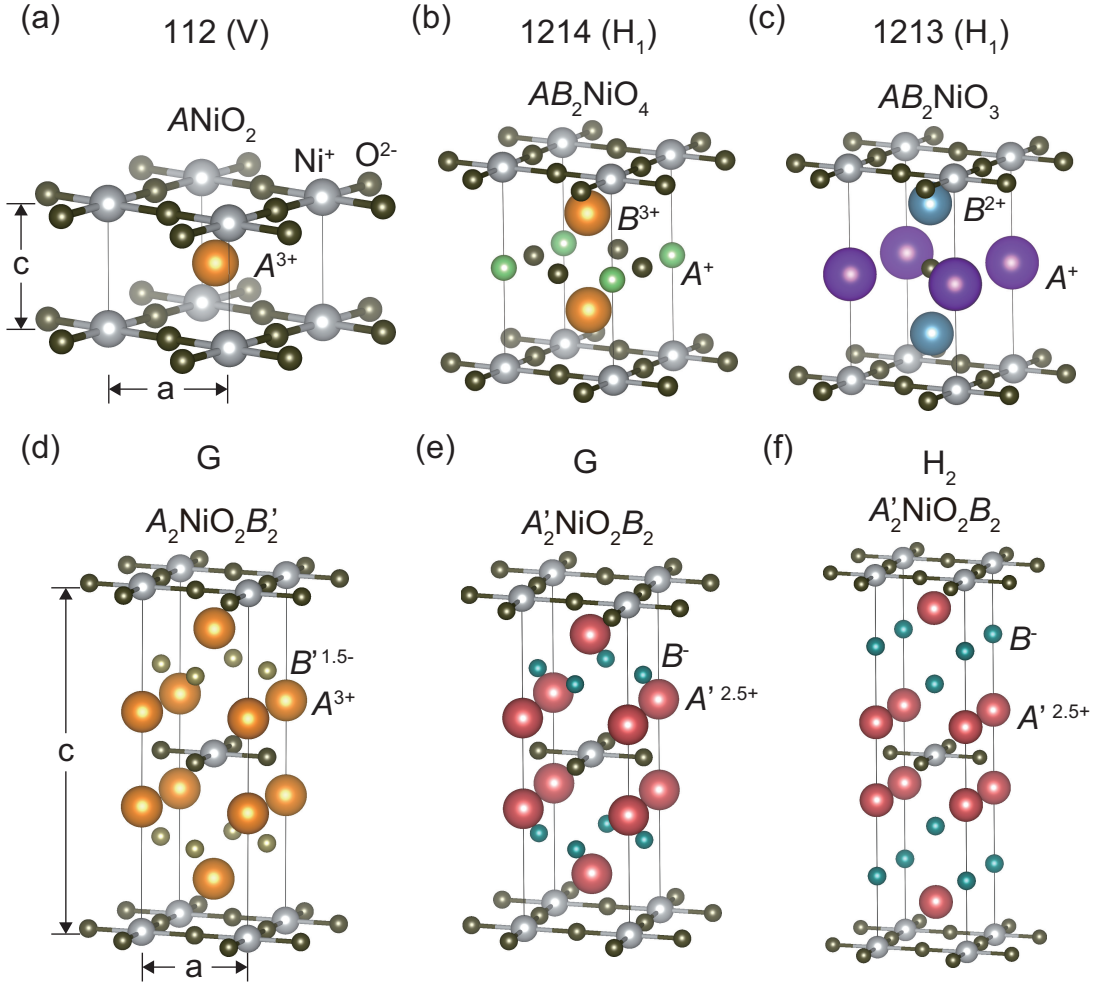


FIG. 3. Crystal structures of layered Ni  $d^9$  oxides studied in the present study: (a)  $\text{ANiO}_2$ , (b)  $\text{AB}_2\text{NiO}_4$ , (c)  $\text{AB}_2\text{NiO}_3$ , (d)  $\text{A}_2\text{NiO}_2\text{B}'_2$ , (e)  $\text{A}'_2\text{NiO}_2\text{B}_2$  (G block), and (f)  $\text{A}'_2\text{NiO}_2\text{B}_2$  ( $\text{H}_2$  block). For  $\text{A}_2\text{NiO}_2\text{B}'_2$ , a half of  $\text{B}'$  sites are occupied by  $\text{O}^{2-}$  and the other half are occupied by  $\text{F}^-$  or  $\text{H}^-$  (e.g.  $\text{O}_{0.5}\text{F}_{0.5}$ ). Another possibility is 3/4 of  $\text{B}'$  sites are occupied by  $\text{O}^{2-}$  and 1/4 are vacant sites. For  $\text{A}'_2\text{NiO}_2\text{B}_2$  in the G and  $\text{H}_2$  families, a half of  $\text{A}'$  sites are occupied by a cation with a valence of 2+ and the other half are occupied by a 3+ cation (e.g.  $\text{Ba}_{0.5}\text{La}_{0.5}$ ), or 5/6 are occupied by a 3+ cation and 1/6 are vacant sites.

## V. DYNAMICAL STABILITY

In the previous section, we have systematically generated 57 new layered nickelates following our design principles. To assess the dynamical stability of these 57 layered nickelates of Table I, here we perform *ab initio* phonon calculations of these structures. The calculated phonon dispersion curves of 57 nickelates are shown in Fig. 4, where the curves of 16 dynamically stable materials are shown with blue lines.

Among the explored 1214-family nickelates, only  $\text{LiNd}_2\text{NiO}_4$  and  $\text{LiLa}_2\text{NiO}_4$  are predicted to be dynamically stable, as shown in Fig. 4(a). For the  $A$  site cation,  $\text{Li}^{1+}$  is preferable because its ionic radius is the closest to that of  $\text{Ni}^{1+}$ , resulting in a good matching of the in-plane lattice constant between the  $\text{NiO}_2$  and  $\text{LiO}_2$  layers (see Fig. 3(b)). With increasing the  $A$  site ionic radius, the

instability of phonon modes enhances due to the increase in the lattice mismatch. When  $A = \text{Li}$ , the structure becomes dynamically stable if the  $B$  site cation is either Nd or La. This result is reasonable because the ionic radii of  $\text{Nd}^{3+}$  and  $\text{La}^{3+}$  are similar. Since the ionic radius of  $\text{Y}^{3+}$  is also similar to that of  $\text{Nd}^{3+}$  but somewhat smaller,  $\text{LiY}_2\text{NiO}_4$  has unstable phonon modes around the  $\Gamma$  and M points. These soft modes respectively correspond to the distortion of the oxygen atoms in the in-plane and out-of-plane directions. Since the instability of these soft modes is rather weak, applying tensile or compressive strain to  $\text{LiY}_2\text{NiO}_4$ , for example, by growing it on a substrate, may stabilize the  $P4/mmm$  structure.

Figure 4(b) shows the calculated phonon dispersion curves of the 1213-family nickelates. The dynamical stability is realized when  $A = \text{K}$  or  $\text{Rb}$  and  $B = \text{Ca}$ ,  $\text{Sr}$ ,  $\text{Ba}$ , or  $\text{Yb}$ . In contrast with the 1214 family, a relatively



TABLE I. List of layered nickelates explored in this study.

Family	Block layer	Space group	Composition	Structure
112	V	$P4/mmm$	$ANiO_2$ ( $A = \text{La, Nd}$ )	Fig. 3(a)
1214	H <sub>1</sub>	$P4/mmm$	$AB_2NiO_4$ ( $A = \text{Li, Na, K, Rb, Cs}$ ; $B = \text{Y, Sc, La, Nd}$ )	Fig. 3(b)
1213	H <sub>1</sub>	$P4/mmm$	$AB_2NiO_3$ ( $A = \text{Li, Na, K, Rb, Cs}$ ; $B = \text{Mg, Ca, Sr, Ba, Yb}$ )	Fig. 3(c)
G	G	$I4/mmm$	$A_2NiO_2B'_2$ ( $A = \text{Y, La, Nd, Lu}$ ; $B' = \text{O}_{0.5}\text{F}_{0.5}$ )	Fig. 3(d)
			$A'_2NiO_2B_2$ ( $A' = \text{Ba}_{0.5}\text{La}_{0.5}$ ; $B = \text{F, Cl, Br, I}$ )	Fig. 3(e)
H <sub>2</sub>	H <sub>2</sub>	$I4/mmm$	$A'_2NiO_2B_2$ ( $A' = \text{Ba}_{0.5}\text{La}_{0.5}$ ; $B = \text{F, Cl, Br, I}$ )	Fig. 3(f)

large cation is preferred for the  $A$  site in the 1213 family because the number of atoms in the  $AO$  layer is less than that of the  $NiO_2$  layer. The structures with Cs become unstable probably because the ionic radius of  $\text{Cs}^+$  is too large for the  $A$  site. When  $A = \text{K}$  or  $\text{Rb}$ , the structure is stable if  $B$  site is either  $\text{Ca}$ ,  $\text{Sr}$ ,  $\text{Ba}$ , or  $\text{Yb}$ . The ionic radii of  $\text{Ca}^{2+}$  and  $\text{Sr}^{2+}$  are close to those of  $\text{Nd}^{3+}$  and  $\text{La}^{3+}$  which are used as the V block in the stable 112 family. When  $B = \text{Mg}$ , the structure becomes unstable irrespective of types of the  $A$  site cation, which can be attributed to the small ionic radius of  $\text{Mg}^{2+}$ . Also, the large electronegativity of  $\text{Mg}$ , which is larger than that of the other alkaline earth elements, tends to hamper the formation of a stable  $\text{Mg}^{2+}$  cation.

Among the studied four G-family  $A_2NiO_2B'_2$  nickelates,  $\text{La}_2NiO_2B'_2$  and  $\text{Nd}_2NiO_2B'_2$  are predicted to be dynamically stable, and the other two compositions are unstable. This result is again reasonable considering that  $\text{LaNiO}_2$  and  $\text{NdNiO}_2$  have been synthesized, whereas the other two have not been reported so far. Since the ionic radii of  $\text{Y}^{3+}$  and  $\text{Lu}^{3+}$  are somewhat smaller than that of  $\text{Nd}^{3+}$ , the phonon mode around the X and P points, which involves in-plane distortion of the oxygen and  $B'$  atoms, become unstable and the  $I4/mmm$  structure changes into a lower-symmetry structure.

Next, we discuss the dynamical stability of the G-family (T'-type structure) and H<sub>2</sub>-family (T-type structure)  $A'_2NiO_2B_2$  nickelates. As can be seen in the right panels of Fig. 4(c) and the panels of Fig. 4(d), the dynamically stable structure changes clearly depending on the halogen atoms; the G-type structure is stable only when  $B = \text{F}$ , while the H<sub>2</sub>-type structure is stable when  $B = \text{Cl, Br, or I}$ . Interestingly, our computational prediction is consistent with the experimental findings on the related compounds. For example,  $\text{Sr}_2\text{CuO}_2\text{F}_2$  and  $\text{Ba}_2\text{PdO}_2\text{F}_2$  crystallize in the G-type structure [33, 34], whereas  $\text{Sr}_2\text{CuO}_2\text{Cl}_2$  and  $\text{Ba}_2\text{PdO}_2\text{Cl}_2$  display the H<sub>2</sub>-type structure [35–37]. We can infer from these consistent results that the H<sub>2</sub>-type structure tends to become more stable than the G-type structure with increasing the halogen ion radius.

Our systematic *ab initio* phonon calculations predict that 16 compositions out of 57 are dynamically stable. The dynamically stable compositions are  $\text{LiNd}_2\text{NiO}_4$ ,

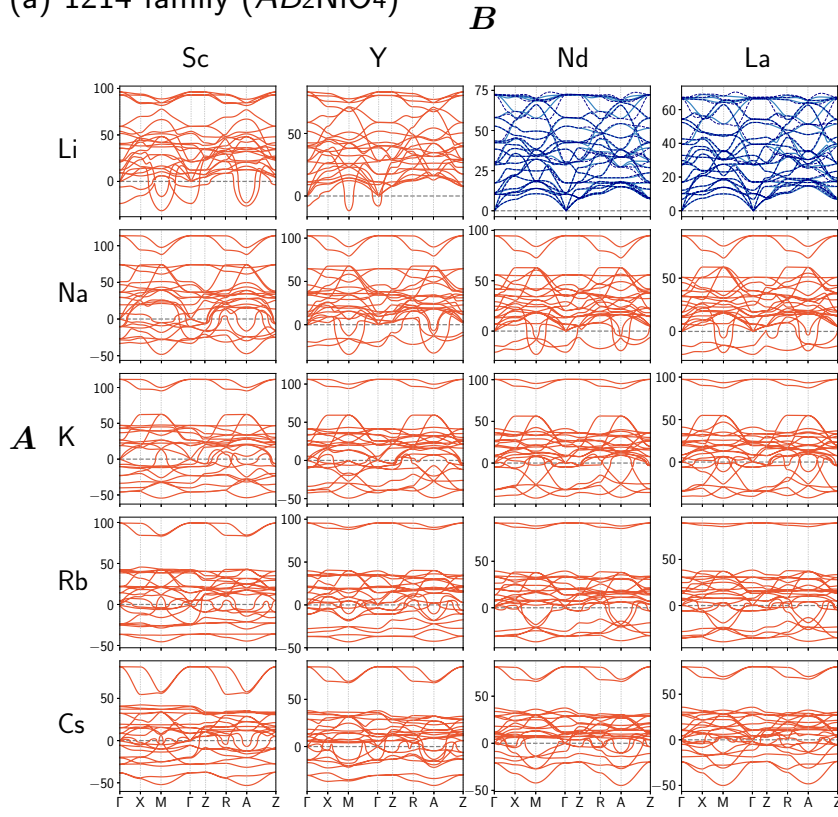
$\text{LiLa}_2\text{NiO}_4$ ,  $AB_2NiO_3$  with  $A = (\text{K, Rb})$  and  $B = (\text{Ca, Sr, Ba, Yb})$ ,  $\text{La}_2NiO_2B'_2$  and  $\text{Nd}_2NiO_2B'_2$  where  $B' = \text{O}_{0.5}\text{F}_{0.5}$ , G-family  $A'_2NiO_2B_2$ , and H<sub>2</sub>-family  $A'_2NiO_2B_2$  ( $B = \text{Cl, Br, I}$ ) with  $A' = \text{Ba}_{0.5}\text{La}_{0.5}$ . Although the dynamical stability does not guarantee the synthesizability of materials, dynamically stable materials are, at least, metastable. Indeed, metastable phases appear ubiquitously [38]. Therefore, we believe that the predicted metastable nickelates can be synthesized by using experimental techniques, including the high-pressure synthesis and the pulsed laser deposition.

## VI. ELECTRONIC STRUCTURE

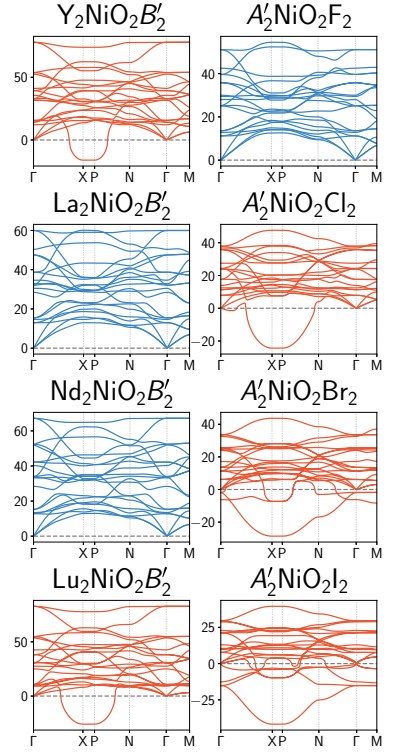
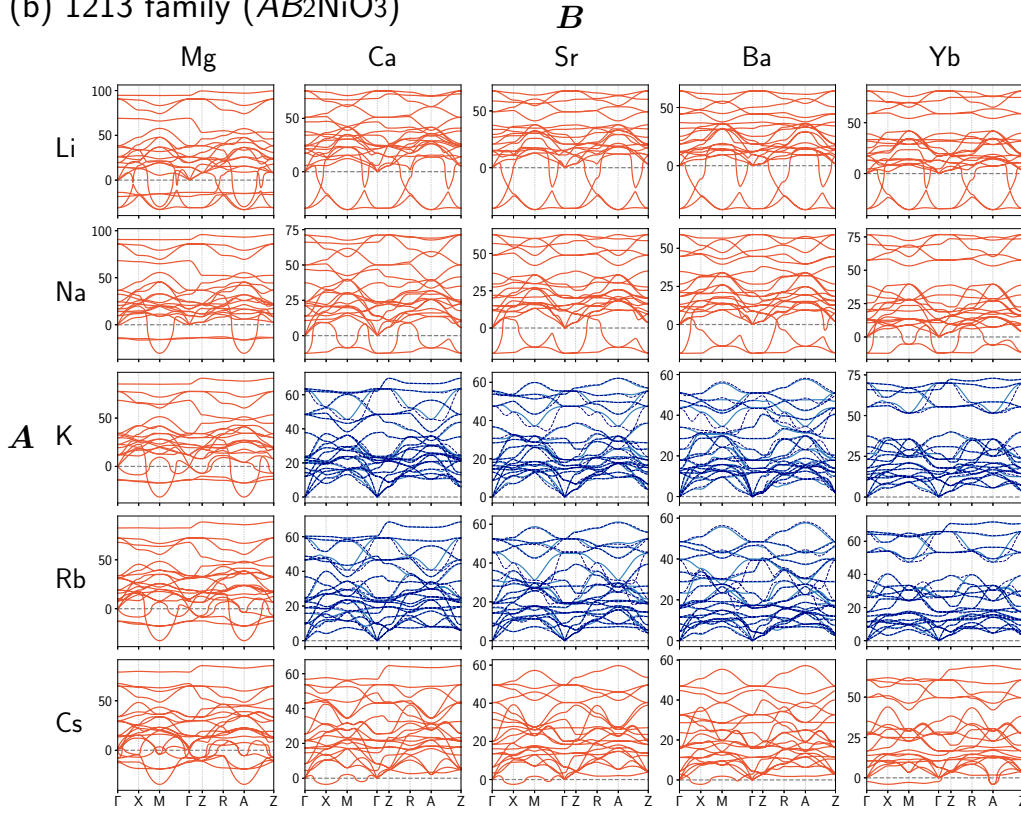
Let us now move on to the electronic structure of the compounds that are shown to be dynamically stable in the previous section. Here, we discuss how the position of the bonding band between the interstitial  $s$  and the cation  $d_{xy}$  orbitals that makes a large extra Fermi pocket in the 112 family changes when adopting the different types of BLs. To this end, we show the electronic band structures calculated for 10 representative dynamically-stable systems in Fig. 5. For each material, we indicate the position of the band minimum of the bonding band, which occurs at  $(k_x, k_y) = (\pi, \pi)$ , by open circles. We see in the figure that the energy level of the bonding band is lifted from that of the 112 family for the all new nickelates.

To see this point more quantitatively, we compare the energy levels of the bonding band in Fig. 6. Intriguingly, the nickelates belonging to the H<sub>2</sub> family are the most promising in that the energy level of the bonding band is significantly higher than the Fermi level, and only the  $\text{Ni } 3d_{x^2-y^2}$  band makes the Fermi surface. See Table XI in Appendix D for the detail of the onsite level of the interstitial  $s$  and cation  $d_{xy}$  orbitals, and the bandwidth of bonding and antibonding bands. In what follows, we look into the detail of the electronic structure of the four families.

Figure 5(a) shows the electronic band structure of  $\text{LiNd}_2\text{NiO}_4$ . We also show the Wannier function originating from the  $\text{Ni } 3d_{x^2-y^2}$  orbital in Fig. 5(b), which is the basis of the effective single-orbital model discussed

(a) 1214 family ( $AB_2NiO_4$ )

(c) G family

(b) 1213 family ( $AB_2NiO_3$ )

(d) H2 family

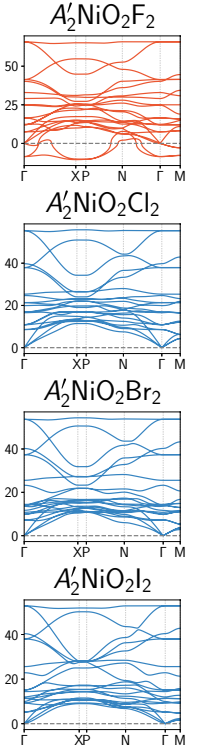


FIG. 4. Phonon dispersion curves of the (a) 1214-family, (b) 1213-family, (c) G-family, and (d) H<sub>2</sub>-family nickelates calculated with the PBEsol functional. We take  $A'$  and  $B'$  atoms to be  $Ba_{0.5}La_{0.5}$  and  $O_{0.5}F_{0.5}$ , respectively. The unit of the vertical axes is meV. For the 1214 and 1213 families, the results based on the  $2 \times 2 \times 2$  and  $4 \times 4 \times 2$  supercells are shown with solid and dashed lines, respectively. Different colors are used for dynamically stable (blue) and unstable (red) compositions.

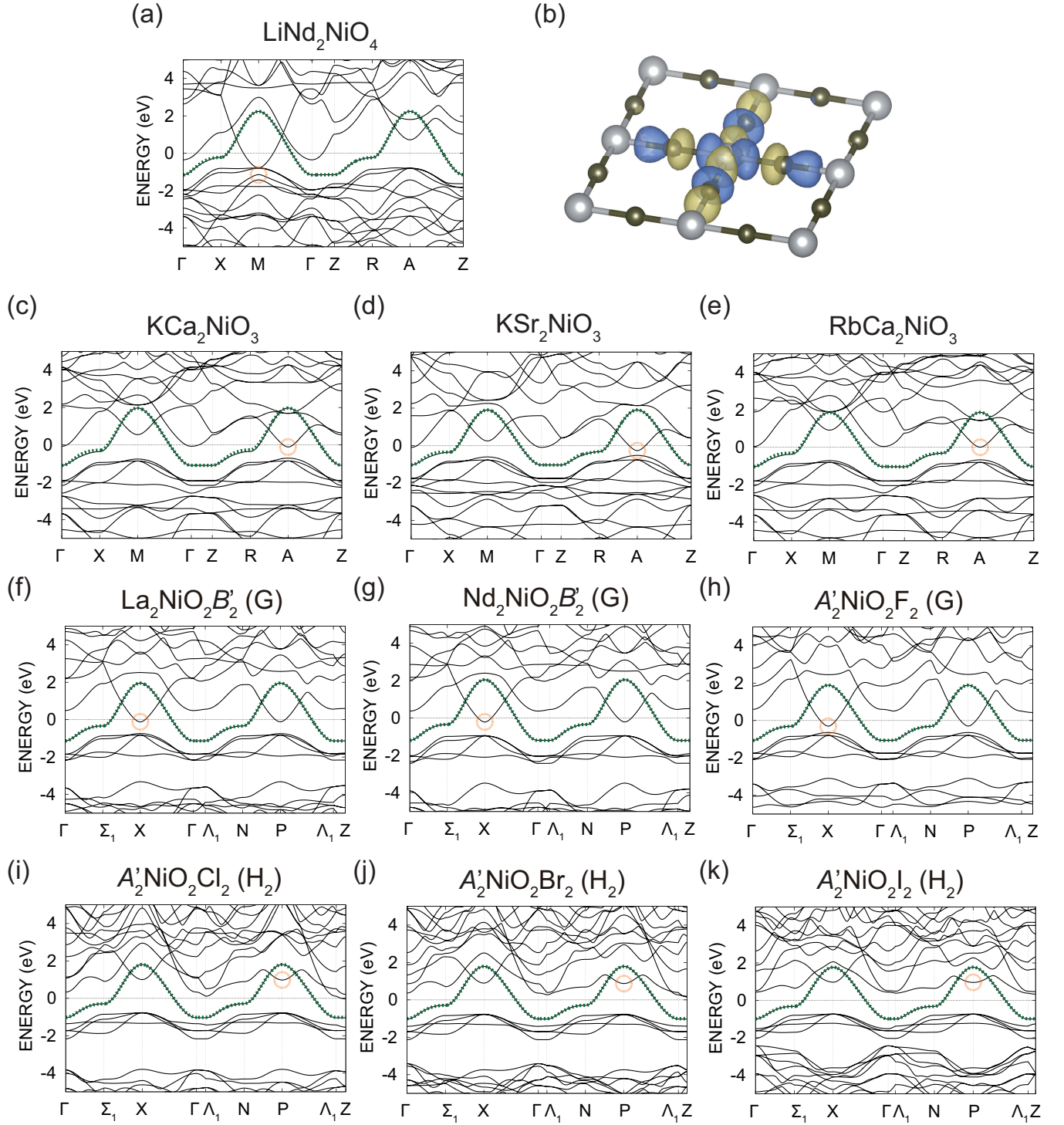


FIG. 5. (a) Electronic band structure of  $\text{LiNd}_2\text{NiO}_4$ . (b) Wannier function of the Ni  $d_{x^2-y^2}$  orbital in  $\text{LiNd}_2\text{NiO}_4$ . (c)–(k) Electronic band structures of  $\text{KCa}_2\text{NiO}_3$ ,  $\text{KSr}_2\text{NiO}_3$ ,  $\text{RbCa}_2\text{NiO}_3$ ,  $\text{La}_2\text{NiO}_2B'_2$ ,  $\text{Nd}_2\text{NiO}_2B'_2$ ,  $A'_2\text{NiO}_2\text{F}_2$ ,  $A'_2\text{NiO}_2\text{Cl}_2$ ,  $A'_2\text{NiO}_2\text{Br}_2$ , and  $A'_2\text{NiO}_2\text{I}_2$ , respectively. The energy is measured from the Fermi level.  $\Sigma_1$  and  $\Lambda_1$  in the  $I4/mmm$  structures are (0.5,0,0) and (0,0,0.5) for the conventional unit cell shown in Fig. 3, respectively. The open circles indicate the band minimum of the bonding band formed by the interstitial  $s$  state and the  $d_{xy}$  state of the neighboring cation. The green dotted curves are the Wannier-interpolated band of the effective single-band model.



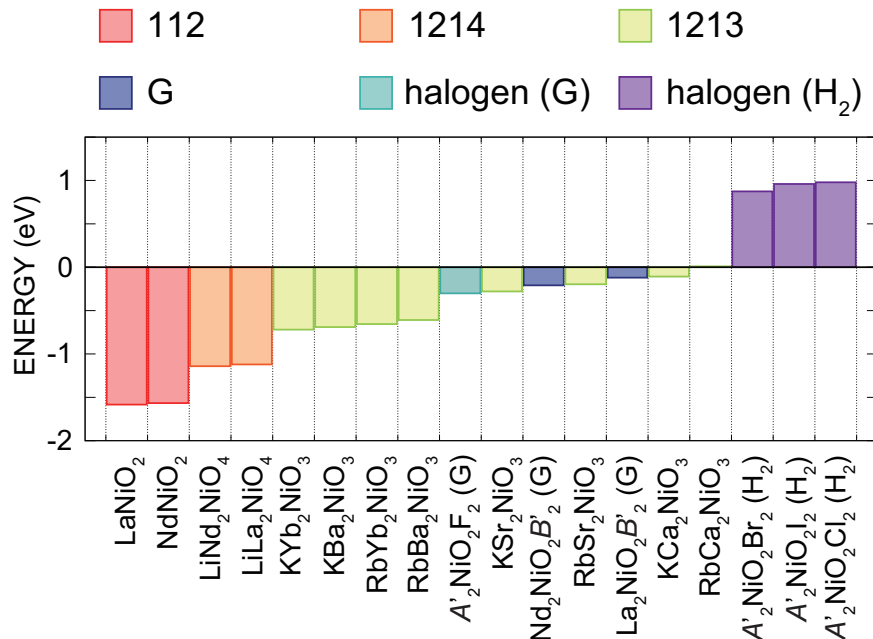


FIG. 6. Lowest energy of the bonding band made from the interstitial  $s$  and the cation  $d_{xy}$  orbitals with respect to the Fermi level.

in Sec. VII. The bottom of the bonding band made from the interstitial  $s$  and the Nd  $5d_{xy}$  orbitals (indicated by the orange circle) is higher than that in the 112 family by 450 meV (see also Fig. 6). However, this bonding band still makes rather large Fermi pockets.

In the 1213 family, the trivalent ions (i.e.,  $\text{La}^{3+}$  and  $\text{Nd}^{3+}$ ) used in the 1214 family are replaced with the divalent ions (i.e.,  $\text{Ca}^{2+}$  and  $\text{Sr}^{2+}$ ). Then, the energy level of the cation  $d_{xy}$  orbital becomes higher, which makes the energy of the bonding state higher. Also, because the  $3d_{xy}$  orbital in  $\text{Ca}^{2+}$  and  $4d_{xy}$  orbital in  $\text{Sr}^{2+}$  are spatially more localized than  $5d_{xy}$  orbital in  $\text{La}^{3+}$  and  $\text{Nd}^{3+}$ , the bandwidth of the bonding and antibonding bands becomes small, resulting in a smaller Fermi pocket. Indeed, in the 1213 family, the BL makes almost no extra Fermi pocket (see Figs. 5(c)–(e) and 6). In particular, in  $\text{RbCa}_2\text{NiO}_3$ , the extra Fermi pocket does not exist, so that the Fermi surface originates only from the Ni  $3d_{x^2-y^2}$  orbital.

We show the electronic band structures of the G-family  $\text{La}_2\text{NiO}_2\text{B}'_2$ ,  $\text{Nd}_2\text{NiO}_2\text{B}'_2$ , and  $\text{A}'_2\text{NiO}_2\text{F}_2$  in Figs. 5(f), (g), and (h), respectively. The size of the Fermi pocket formed by the bonding band is again smaller compared to the 112 family. In the case of the 112 family, the interstitial  $s$  orbital is surrounded by cations. On the other hand, in the G family, the negatively charged halogen site is located near the interstitial  $s$  orbital, which makes the energy of the interstitial  $s$  higher. In  $\text{La}_2\text{NiO}_2\text{B}'_2$ ,  $\text{Nd}_2\text{NiO}_2\text{B}'_2$ , this leads to large energy difference between the interstitial  $s$  and  $d_{xy}$  orbitals, and the hybridization between the two orbitals becomes smaller. Therefore, the bonding-antibonding splitting is much smaller than that of  $\text{NdNiO}_2$ , and consequently, the Fermi pocket formed

by the bonding band becomes small. In the case of  $\text{A}'_2\text{NiO}_2\text{F}_2$  with  $\text{A}' = \text{Ba}_{0.5}\text{La}_{0.5}$ , the energy level of the  $5d_{xy}$  orbital also rises because of the change of the valence of the cation from  $3+$  to  $2.5+$ . This also leads to a smaller Fermi pocket even though the bonding-antibonding splitting is comparable to that of the 112 family.

We also show the electronic band structures of  $\text{A}'_2\text{NiO}_2\text{Cl}_2$ ,  $\text{A}'_2\text{NiO}_2\text{Br}_2$ , and  $\text{A}'_2\text{NiO}_2\text{I}_2$  belonging to the  $\text{H}_2$  family (Figs. 5(i), (j) and (k)). These materials have no Fermi pocket originating from the bonding band. The energy level of the interstitial  $s$  orbital in the  $\text{H}_2$  family is very high. This is because the negatively-charged halogen site is located just on top of the interstitial site; thus the increase in the onsite level of the interstitial  $s$  orbital is even larger than that of the G family.

The energy minimum of the bonding state formed by the interstitial  $s$  and  $d_{xy}$  orbitals is summarized in Fig. 6. When the energy minimum is lower, the size of the Fermi pocket made by the bonding band is larger. We see that the energy minimum is highest for the  $\text{H}_2$  family and lowest for  $\text{LaNiO}_2$ . Our results indicate that the  $\text{H}_2$  family would provide a firm ground to study the possibility of high- $T_c$  superconductivity in the Mott-Hubbard regime of the Zaanen-Sawatzky-Allen classification [39].

## VII. EFFECTIVE SINGLE-ORBITAL MODEL

As we have discussed in the previous sections, our proposed materials are closer to an ideal  $d^9$  system compared to  $\text{NdNiO}_2$ . Then, the electronic structure around the Fermi level is well described by the single-orbital model in the Mott-Hubbard regime. Here, we construct effective



TABLE II. Hopping and interaction parameters in the single-orbital model.  $t$ ,  $t'$ ,  $t''$  are the nearest, next-nearest, and third-nearest hopping integrals, respectively.  $U$  is the onsite Hubbard interaction. The energy unit is eV. The data for  $\text{NdNiO}_2$  are taken from Ref. 8.

Composition	Family	$t$	$t'$	$t''$	$U$	$ U/t $	$t'/t$
$\text{NdNiO}_2$	112	-0.370	0.092	-0.045	2.608	7.052	-0.250
$\text{LiNd}_2\text{NiO}_4$	1214	-0.404	0.099	-0.052	2.865	7.086	-0.245
$\text{KCa}_2\text{NiO}_3$	1213	-0.370	0.104	-0.049	3.222	8.701	-0.280
$\text{KSr}_2\text{NiO}_3$	1213	-0.357	0.102	-0.048	2.985	8.366	-0.285
$\text{RbCa}_2\text{NiO}_3$	1213	-0.352	0.100	-0.046	3.347	9.522	-0.284
$\text{Nd}_2\text{NiO}_2B'_2$	G	-0.389	0.098	-0.049	3.241	8.335	-0.253
$A'_2\text{NiO}_2\text{F}_2$	G	-0.355	0.095	-0.045	3.399	9.587	-0.269
$A'_2\text{NiO}_2\text{Br}_2$	H <sub>2</sub>	-0.337	0.089	-0.039	3.586	10.637	-0.263
$\text{RbSr}_2\text{PdO}_3$	1213	-0.493	0.116	-0.076	2.362	4.795	-0.236
$A'_2\text{PdO}_2\text{Cl}_2$	G	-0.443	0.097	-0.063	2.699	6.085	-0.218

single orbital models for the  $d^9$  candidate nickelates by using a combination of the maximally localized Wannier functions [40, 41] and the constrained random phase approximation (cRPA) [42]. The detail of the calculations can be found in Appendix A 4.

Table II shows the hopping and interaction parameters of the single-orbital model. The band dispersion curves obtained by the constructed tight-binding Hamiltonians well reproduce those of the density functional theory calculations (see Fig. 5). The property of the single-orbital model is summarized as follows:

- All the materials are in the strongly correlated regime:  $|U/t|$  is around 7–11. Correlation strength is comparable to that of the cuprates [8, 43–48].
- The values of frustration parameter  $t'/t$  lie between -0.29 and -0.24, which are also comparable to those of the cuprates [2, 8, 49].
- Materials with large in-plane lattice constant tends to have small hopping integral  $t$ .
- When the cation-layer bonding orbital forms a Fermi pocket, it contributes to the screening of the Coulomb interaction, although the effect is not drastic to make the system weakly correlated [8]. Therefore, when such a Fermi pocket is small or eliminated, the Hubbard  $U$  tends to become large. In particular, the H<sub>2</sub>-family nickelates have the most isolated Ni  $3d_{x^2-y^2}$  band; therefore, they have the strongest electron correlations.

## VIII. MATERIALS DESIGN OF PALLADATE ANALOGUE OF HIGH $T_c$ CUPRATES

Let us finally extend the above discussion to a systematic materials design of layered palladates with the  $d^9$  configuration. The correlation strength would be weaker than that of nickelates; hence, by combining nickelates

and palladates, we might be able to study a wide range of the  $|U/t|$  parameter region.

To seek dynamically stable  $d^9$  layered palladates, we first optimized the structure parameters of the 57 palladates and then performed systematic phonon calculations. See Appendix C for the details of the methods. We see in Fig. 9 that only 6 compositions out of 57 are predicted to be dynamically stable. The stable compositions are  $\text{ASr}_2\text{PdO}_3$  ( $A = \text{K, Rb, Cs}$ ),  $\text{CsBa}_2\text{PdO}_3$ , and G-type  $A'_2\text{PdO}_2B_2$  ( $B = \text{F, Cl}$ ). Because Pd has a larger atomic radius than Ni, the structure tends to be stable when the elements in the BLs have a larger atomic radius compared to those in nickelates.

The electronic band structures of  $\text{RbSr}_2\text{PdO}_3$  in the 1213 family,  $A'_2\text{PdO}_2\text{F}_2$  and  $A'_2\text{PdO}_2\text{Cl}_2$  in the G family are shown in Figs. 7(a), (b), and (c), respectively. The band structure of  $\text{RbSr}_2\text{PdO}_3$  and  $A'_2\text{PdO}_2\text{Cl}_2$  have no extra Fermi surface originating from the interstitial  $s$  and  $d_{xy}$  orbitals. The bandwidth of the Pd compounds is larger than that of the Ni compounds as expected.

As in the nickelates, we construct effective single-orbital models for the palladates. The Wannier interpolated bands can be found in Fig. 7. The hopping and interaction parameters are shown in Table II. We see that:

- The kinetic energy scale is larger than that of nickelates.
- $|U/t|$  in the palladates is smaller compared to that of nickelates because of the extended  $4d$  orbitals making  $U$  smaller and  $t$  larger. Hence, the correlation strength is weaker.  $|U/t|$  is around 5–6.
- Material dependence of the correlation strength is the same as that of nickelates; when the Fermi pocket formed by the cation-layer bonding state is small or eliminated, the Hubbard  $U$  tends to become large. In particular, the Hubbard  $U$  in the G-type  $A'_2\text{PdO}_2\text{Cl}_2$  is comparable to that of  $\text{NdNiO}_2$ .

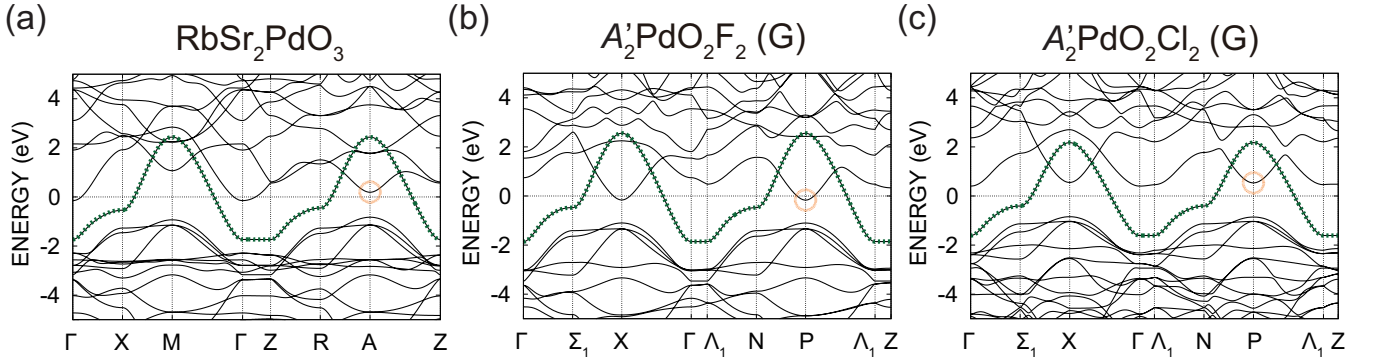


FIG. 7. (a)–(c) Electronic band structures of RbSr<sub>2</sub>PdO<sub>3</sub>, A'<sub>2</sub>PdO<sub>2</sub>F<sub>2</sub>, and A'<sub>2</sub>PdO<sub>2</sub>Cl<sub>2</sub>, respectively. The energy is measured from the Fermi level. The open circles indicate the band minimum of the bonding band formed by the interstitial *s* state and the *d<sub>xy</sub>* state of the neighboring cation. The green dotted curves are the Wannier-interpolated band of the effective single-band model.

## IX. SUMMARY

We performed a systematic computational search for layered nickelates that are dynamically stable and whose electronic structure better mimics that of high- $T_c$  cuprates than Sr-doped NdNiO<sub>2</sub>. While there is more than 10% self-doping of the Ni  $3d_{x^2-y^2}$  orbital in NdNiO<sub>2</sub>, by referring to the work by Tokura and Arima [21] for high- $T_c$  cuprates, and by performing comprehensive phonon calculations, we found new dynamically-stable layered nickelates where the self-doping is almost or completely suppressed. We derived effective single-band models for the promising materials and found that they are in the strongly correlated regime:  $|U/t|$  is around 7–11. By replacing Ni with Pd, we also designed promising palladate analogues of high- $T_c$  cuprates. Once synthesized, these materials will provide a firm ground for studying the possibility of high- $T_c$  superconductivity in the Mott-Hubbard regime of the Zaanen-Sawatzky-Allen classification [39].

## ACKNOWLEDGMENTS

We are grateful to Y. Tokura, T. Katase, M. Uchida, Y. Taguchi, S. Ishiwata, and S. Seki for their helpful comments and to K. Nakamura and Y. Yoshimoto for fruitful discussion. We acknowledge the financial support of JSPS Kakenhi Grant No. 16H06345 (MH, TT, YN, and RA), No. 17K14336 (YN), No. 18H01158 (YN), and No. 19H05825 (RA). The figures of the crystal structures are created by the VESTA software [50].

MH and TT contributed equally to this work.

## Appendix A: Details of computational methods

### 1. Structural optimization

The structure optimization of the 1214- and 1213-family nickelates was performed with the Vienna *Ab initio* Simulation Package (VASP) [51]. We used the projector augmented wave (PAW) [52, 53] potential sets recommended by VASP and set the kinetic energy cutoff to 600 eV for systems containing Li and 500 eV for the others. For the G- and H<sub>2</sub>-family nickelates, the structure optimization was conducted by using QUANTUM ESPRESSO (QE) [54] with the optimized norm-conserving Vanderbilt (ONCV) pseudopotentials [55] adopted from the Pseudo-Dojo [56]. Mixed pseudopotentials of Ba<sub>0.5</sub>La<sub>0.5</sub> and O<sub>0.5</sub>F<sub>0.5</sub>, generated based on the virtual crystal approximation (VCA), were used for representing the cation A' and the anion B', respectively. The kinetic cutoff energy of 100 Ry was employed in the QE calculations. For both VASP and QE calculations, the  $\mathbf{k}$  point mesh was generated automatically in such a way that the mesh density in the reciprocal space becomes larger than 450 Å<sup>-3</sup>. Also, 4*f* electrons of Nd and Lu were frozen in the core. Since phonon frequencies are rather sensitive to the lattice parameters, we employed the generalized-gradient approximation (GGA) with the Perdew-Burke-Ernzerhof parameterization for solid (PBEsol) [57], which is reported to work well for predicting lattice parameters of oxides and other solids [58, 59]. The complete information of the optimized crystal structures is summarized in Appendix B and C.

### 2. Phonon calculation

The phonon calculations of the 57 layered nickelates were performed by computing second-order interatomic

force constants with sufficiently large supercells. For quickly identifying dynamically stable compositions of the 1214 and 1213 families, we started the phonon calculations with  $2 \times 2 \times 2$  supercells, which contain 64 (56) atoms for the 1214 (1213) family. For each nickelate, the dynamical stability is assessed from the presence of unstable phonon modes; if an unstable phonon mode ( $\omega_{\mathbf{q}\nu}^2 < 0$ ) exists on the commensurate  $2 \times 2 \times 2$   $\mathbf{q}$  points, the composition is dynamically unstable and therefore excluded from the candidate list. After the first quick screening based on  $2 \times 2 \times 2$  supercells, we performed a second screening based on  $4 \times 4 \times 2$  supercells for confirming the dynamical stability of the candidate compositions. Since the number of explored composition is relatively few for the G- and  $H_2$ -family, we only employed  $3 \times 3 \times 1$  conventional cells, which contain 126 atoms and therefore are sufficiently large, for judging the dynamical stability of the G- and  $H_2$ -type nickelates. All of the phonon calculations were conducted by using ALAMODE software [60, 61].

### 3. Band structure calculation

The band structures and the maximally-localized Wannier functions (MLWFs) shown in Sec. VI are obtained by using the *ab initio* code OpenMX [22]. We employed the valence orbital sets Li8.0-*s3p3d2*, K10.0-*s4p3d2*, Rb11.0-*s3p3d2f2*, Cs12.0-*s3p2d2f2*, Ca9.0-*s4p3d2*, Sr10.0-*s3p1d2f1*, Ba10.0-*s3p2d2f2*, Yb8.0-*s3p2d2f1*, La8.0-*s3p3d3*, Nd8.0-OC-*s2p2d2f1*, Ni6.0H-*s4p3d2f1*, Pd7.0-*s2p2d2f1*, O-5.0-*s3p3d2*, F6.0-*s2p2d1*, Cl7.0-*s2p2d1*, Br7.0-*s3p2d1*, I7.0-*s3p3d2f1*, 5.0-*s3p3d2* for  $N = 8.5$  virtual atom, and 8.0-*s3p3d2* for  $N = 56.5$  virtual atom. The energy cutoff for the numerical integration was set to 150 Ry. The Wannier functions of the interstitial *s* and cation  $d_{xy}$  orbitals were constructed from the outer energy window of  $[-2 \text{ eV}; 12 \text{ eV}]$  for  $\text{ANiO}_2$  and  $\text{AB}_2\text{NiO}_4$ ,  $[-1 \text{ eV}; 12 \text{ eV}]$  for  $\text{AB}_2\text{NiO}_3$ ,  $\text{A}_2\text{NiOB}'_2$ ,  $\text{AB}_2\text{PdO}_3$ , and  $\text{A}'_2\text{PdO}_2\text{F}_2$ , and  $[0 \text{ eV}; 12 \text{ eV}]$  for  $\text{A}'_2\text{NiO}_2\text{B}_2$  and  $\text{A}'_2\text{PdO}_2\text{Cl}_2$ . The Wannier functions of the  $3d_{x^2-y^2}$  orbital for the Ni compounds were constructed from the outer energy window of  $[-1.5 \text{ eV}; 2.5 \text{ eV}]$ , where we did not use the inner energy window for  $\text{ANiO}_2$  and  $\text{AB}_2\text{NiO}_4$  and used the inner energy window of  $[-0.4 \text{ eV}; -0.3 \text{ eV}]$  for  $\text{KSr}_2\text{NiO}_3$ ,  $[-0.45 \text{ eV}; -0.35 \text{ eV}]$  for  $\text{A}'_2\text{NiO}_2\text{F}_2$ , and  $[-0.35 \text{ eV}; -0.25 \text{ eV}]$  for the other systems. The Wannier functions of the  $4d_{x^2-y^2}$  orbital for the Pd compounds were constructed from the outer energy window of  $[-2 \text{ eV}; 2.5 \text{ eV}]$  for  $\text{KSr}_2\text{PdO}_3$  and  $\text{A}'_2\text{PdO}_2\text{F}_2$ , and  $[-2 \text{ eV}; 3 \text{ eV}]$  for  $\text{A}'_2\text{PdO}_2\text{Cl}_2$ , where we used the inner energy window of  $[-0.6 \text{ eV}; -0.3 \text{ eV}]$  for all the Pd-based compounds. The lattice constants obtained by the VASP and QE calculations, shown in Tables III–X, were used except for  $\text{NdNiO}_3$  and  $\text{LaNiO}_3$ ; for these 112-family nickelates, we used the experimental lattice constants [24, 25]. We employed the  $12 \times 12 \times 12$   $\mathbf{k}$  mesh for the 112 family,  $12 \times 12 \times 8$   $\mathbf{k}$  mesh for all other

families.

### 4. cRPA calculation

The derivation of the single-band effective Hamiltonians shown in Secs. VII and VIII was performed by using RESPACK [62][63]. First, we performed the DFT band structure calculations using QE [54]. We employed Perdew-Burke-Ernzerhof (PBE) [64] norm-conserving pseudopotentials generated by the code ONCVSP (Optimized Norm-Conserving Vanderbilt Pseudopotential) [55], which were downloaded from the PseudoDojo [56]. The kinetic energy cutoff was set to be 100 Ry for the wave functions, and 400 Ry for the charge density. We used  $11 \times 11 \times 7$   $\mathbf{k}$ -mesh for 1213 and 1214 families and  $11 \times 11 \times 11$   $\mathbf{k}$ -mesh for G and  $H_2$  families.

We constructed the maximally localized Wannier functions [40, 41] using RESPACK. The outer energy window was set as follows:

- $\text{LiNd}_2\text{NiO}_4$  (1214):  $[-1.15 \text{ eV}; 2.25 \text{ eV}]$
- $\text{KCa}_2\text{NiO}_3$  (1213):  $[-1.10 \text{ eV}; 2.00 \text{ eV}]$
- $\text{KSr}_2\text{NiO}_3$  (1213):  $[-1.00 \text{ eV}; 1.95 \text{ eV}]$
- $\text{RbCa}_2\text{NiO}_3$  (1213):  $[-1.05 \text{ eV}; 1.90 \text{ eV}]$
- $\text{Nd}_2\text{NiO}_2\text{B}'_2$  (G):  $[-1.15 \text{ eV}; 2.10 \text{ eV}]$
- $\text{A}'_2\text{NiO}_2\text{F}_2$  (G):  $[-1.00 \text{ eV}; 1.95 \text{ eV}]$
- $\text{A}'_2\text{NiO}_2\text{Br}_2$  ( $H_2$ ):  $[-1.05 \text{ eV}; 1.80 \text{ eV}]$
- $\text{RbSr}_2\text{PdO}_3$  (1213):  $[-1.60 \text{ eV}; 2.55 \text{ eV}]$
- $\text{A}'_2\text{PdO}_2\text{Cl}_2$  (G):  $[-1.55 \text{ eV}; 2.20 \text{ eV}]$

For the nickelate of the 1213, G, and  $H_2$  families, we also used the inner window of  $[-0.35 \text{ eV}; 0.25 \text{ eV}]$ . For the palladates, the inner window was set to be  $[-0.45 \text{ eV}; 0.35 \text{ eV}]$ .

The interaction parameters were calculated based on the cRPA method [42], which is implemented in RESPACK. For the band disentanglement, we follow the scheme proposed in Ref. 65. The energy cutoff for the dielectric function was set to be 20 Ry. The total number of bands used in the calculation of the polarization was 160. The maximum energy of the unoccupied bands reaches at least 40 eV with respect to the Fermi level.

### Appendix B: Structural parameters and X-ray diffraction patterns of layered nickelates

The complete list of the structural parameters obtained after the structural optimization based on PBEsol is given in Tables III–VI. In these tables, the dynamically stable compositions are shown in boldface. For some dynamically stable nickelates, the powder X-ray diffraction

patterns are calculated by using VESTA [50] and shown in Fig. 8. X-ray diffraction patterns of the other nickelates can be calculated easily from the structure data shown in the tables.

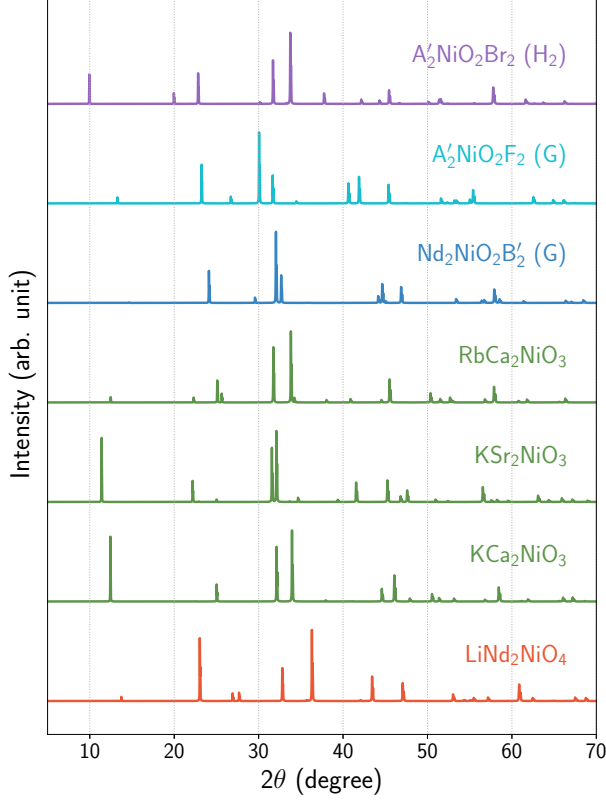


FIG. 8. X-ray powder diffraction patterns of several dynamically stable nickelates calculated by using the optimized structures. Different colors are used for different structural prototypes.

TABLE III. Structural parameters of the  $AB_2NiO_4$  structures ( $P4/mmm$ ) optimized with PBEsol. The fractional coordinates of each atom are as follows:  $A:(0,0,\frac{1}{2})$ ,  $B:(\frac{1}{2},\frac{1}{2},\pm z)$ ,  $Ni:(0,0,0)$ ,  $O:(0,\frac{1}{2},0)$ ,  $(\frac{1}{2},0,0)$ ,  $(\frac{1}{2},0,\frac{1}{2})$ ,  $(0,\frac{1}{2},\frac{1}{2})$ . Dynamically stable compositions are shown in bold.

Composition	$a$ (Å)	$c$ (Å)	$c/a$	$z$
LiSc <sub>2</sub> NiO <sub>4</sub>	3.6725	5.6888	1.5490	0.2628
LiY <sub>2</sub> NiO <sub>4</sub>	3.7799	6.1254	1.6205	0.2596
<b>LiNd<sub>2</sub>NiO<sub>4</sub></b>	3.8584	6.4398	1.6691	0.2587
<b>LiLa<sub>2</sub>NiO<sub>4</sub></b>	3.9035	6.5826	1.6863	0.2584
NaSc <sub>2</sub> NiO <sub>4</sub>	3.8367	5.6984	1.4852	0.2614
NaY <sub>2</sub> NiO <sub>4</sub>	3.9325	6.1000	1.5512	0.2580
NaNd <sub>2</sub> NiO <sub>4</sub>	4.0061	6.3741	1.5911	0.2572
NALa <sub>2</sub> NiO <sub>4</sub>	4.0508	6.4935	1.6030	0.2569
KSc <sub>2</sub> NiO <sub>4</sub>	4.0863	5.6913	1.3928	0.2515
KY <sub>2</sub> NiO <sub>4</sub>	4.1774	6.0825	1.4561	0.2530
KNd <sub>2</sub> NiO <sub>4</sub>	4.2398	6.3125	1.4889	0.2529
KL <sub>2</sub> NiO <sub>4</sub>	4.2813	6.4240	1.5005	0.2538
RbSc <sub>2</sub> NiO <sub>4</sub>	4.1803	5.6927	1.3618	0.2399
RbY <sub>2</sub> NiO <sub>4</sub>	4.2806	6.0507	1.4135	0.2449
RbNd <sub>2</sub> NiO <sub>4</sub>	4.3402	6.2683	1.4442	0.2458
RbLa <sub>2</sub> NiO <sub>4</sub>	4.3769	6.4123	1.4650	0.2458
CsSc <sub>2</sub> NiO <sub>4</sub>	4.3039	5.7331	1.3321	0.2305
CsY <sub>2</sub> NiO <sub>4</sub>	4.3887	6.0389	1.3760	0.2369
CsNd <sub>2</sub> NiO <sub>4</sub>	4.4333	6.2465	1.4090	0.2376
CsLa <sub>2</sub> NiO <sub>4</sub>	4.4588	6.4108	1.4378	0.2366

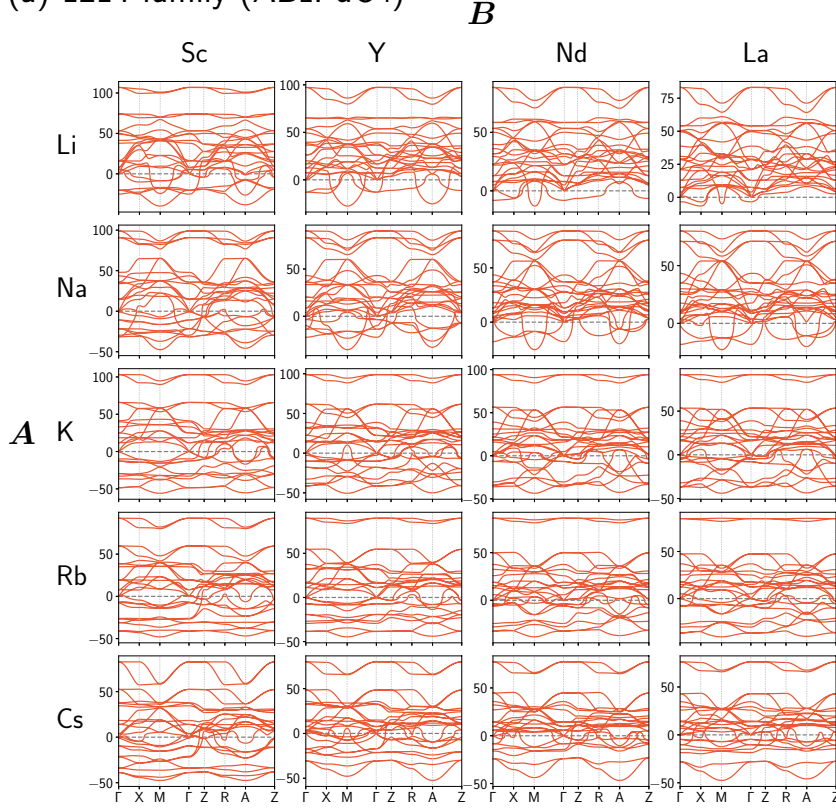
#### Appendix D: Energy of the interstitial $s$ and the cation $d_{xy}$ orbitals

We summarize the energies of the interstitial  $s$  orbital, the cation  $d_{xy}$  orbital, and their bonding/antibonding states for the Ni-based compounds in Table XI and those for the Pd-based compounds in Table XII.

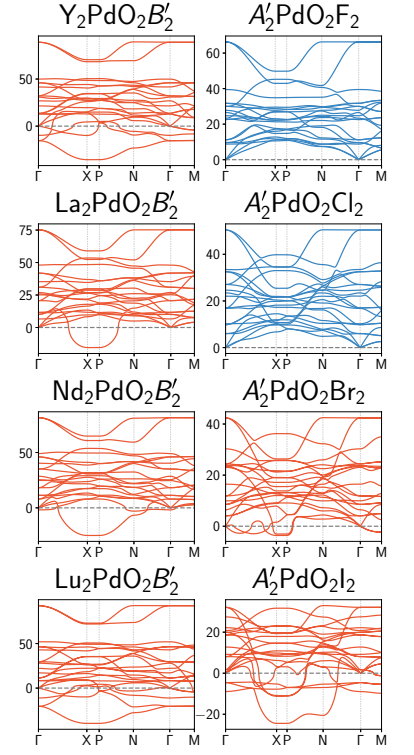
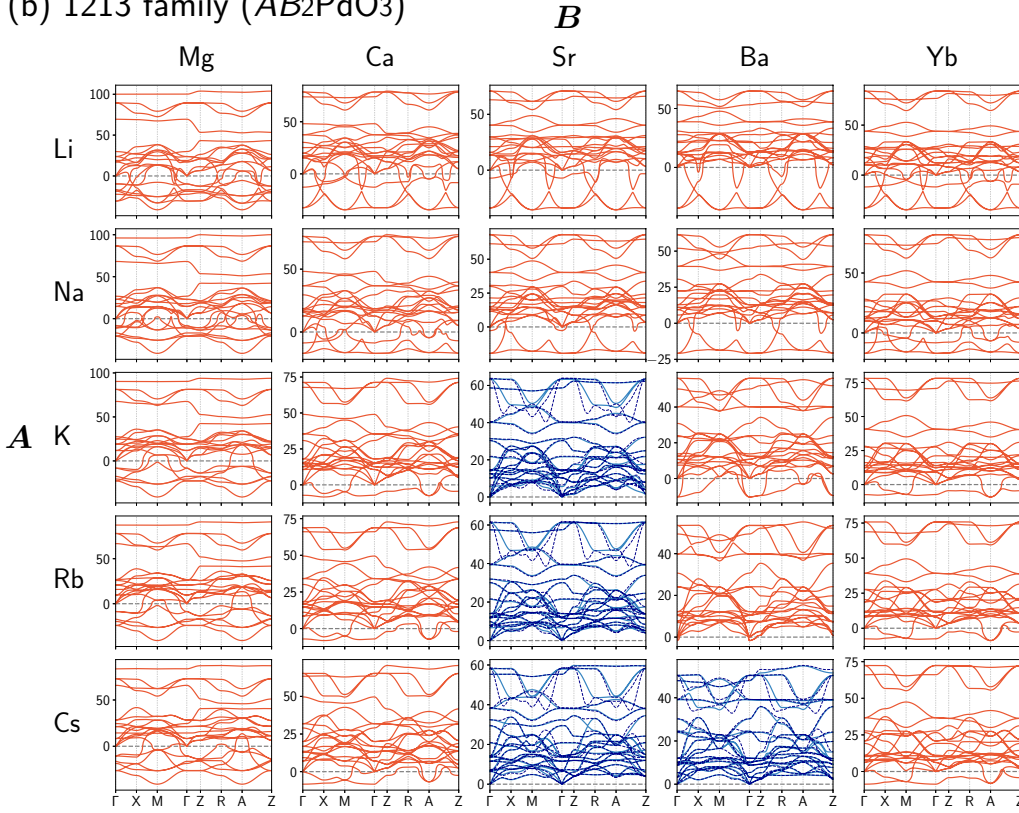
#### Appendix C: Structural parameters and phonons of layered palladates

The structure optimization and phonon calculation of the 57 studied palladates were performed by using exactly the same computational conditions as nickelates described in Appendix A 1 and A 2. The structural parameters of the studied palladates obtained after the structural optimization based on PBEsol are given in Tables VII–X. In these tables, the dynamically stable compositions are shown in boldface. Also, the calculated phonon dispersion curves of the 57 palladates are summarized in Fig. 9.



(a) 1214 family ( $AB_2PdO_4$ )

(c) G family

(b) 1213 family ( $AB_2PdO_3$ )

(d) H2 family

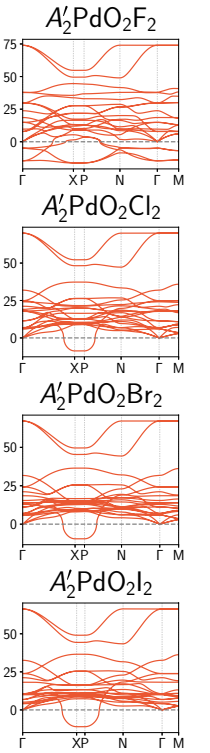


FIG. 9. Phonon dispersion curves of (a) 1214-family, (b) 1213-family, (c) G-family, and (d) H<sub>2</sub>-family palladates calculated based on the PBEsol functional. We take  $A'$  and  $B'$  atoms to be  $Ba_{0.5}La_{0.5}$  and  $O_{0.5}F_{0.5}$ , respectively. The unit of the vertical axes is meV. For the 1214 and 1213 families, results based on the  $2\times 2\times 2$  and  $4\times 4\times 2$  supercells are shown with solid and dashed lines, respectively. Different colors are used for dynamically stable (blue) and unstable (red) compositions.

TABLE IV. Structural parameters of the  $AB_2\text{NiO}_3$  structures ( $P4/mmm$ ) optimized with PBEsol. The fractional coordinates of each atom are as follows:  $A:(0,0,\frac{1}{2})$ ,  $B:(\frac{1}{2},\frac{1}{2},\pm z)$ ,  $\text{Ni}:(0,0,0)$ ,  $\text{O}:(0,\frac{1}{2},0)$ ,  $(\frac{1}{2},0,0)$ ,  $(\frac{1}{2},\frac{1}{2},\frac{1}{2})$ . Dynamically stable compositions are shown in bold.

Composition	$a$ (Å)	$c$ (Å)	$c/a$	$z$
$\text{LiMg}_2\text{NiO}_3$	3.7236	6.2398	1.6757	0.1997
$\text{LiCa}_2\text{NiO}_3$	3.8164	7.1632	1.8770	0.1982
$\text{LiSr}_2\text{NiO}_3$	3.8740	7.8523	2.0269	0.2006
$\text{LiBa}_2\text{NiO}_3$	3.8923	8.6489	2.2221	0.2054
$\text{LiYb}_2\text{NiO}_3$	3.7824	6.8848	1.8202	0.1906
$\text{NaMg}_2\text{NiO}_3$	3.7621	6.2659	1.6655	0.1989
$\text{NaCa}_2\text{NiO}_3$	3.8580	7.1527	1.8540	0.1966
$\text{NaSr}_2\text{NiO}_3$	3.9196	7.8278	1.9971	0.1987
$\text{NaBa}_2\text{NiO}_3$	3.9428	8.6133	2.1846	0.2033
$\text{NaYb}_2\text{NiO}_3$	3.8210	6.8729	1.7987	0.1892
$\text{KMg}_2\text{NiO}_3$	3.8379	6.2828	1.6371	0.1971
<b><math>\text{KCa}_2\text{NiO}_3</math></b>	3.9372	7.1090	1.8056	0.1931
<b><math>\text{KSr}_2\text{NiO}_3</math></b>	4.0047	7.7557	1.9366	0.1948
<b><math>\text{KBa}_2\text{NiO}_3</math></b>	4.0375	8.5135	2.1086	0.1997
<b><math>\text{KYb}_2\text{NiO}_3</math></b>	3.8901	6.8390	1.7581	0.1867
$\text{RbMg}_2\text{NiO}_3$	3.8881	6.2946	1.6189	0.1967
<b><math>\text{RbCa}_2\text{NiO}_3</math></b>	3.9834	7.0911	1.7801	0.1922
<b><math>\text{RbSr}_2\text{NiO}_3</math></b>	4.0513	7.7240	1.9065	0.1937
<b><math>\text{RbBa}_2\text{NiO}_3</math></b>	4.0931	8.4596	2.0668	0.1982
<b><math>\text{RbYb}_2\text{NiO}_3</math></b>	3.9331	6.8240	1.7350	0.1860
$\text{CsMg}_2\text{NiO}_3$	3.9650	6.3041	1.5899	0.1960
$\text{CsCa}_2\text{NiO}_3$	4.0494	7.0750	1.7472	0.1910
$\text{CsSr}_2\text{NiO}_3$	4.1140	7.6947	1.8704	0.1922
$\text{CsBa}_2\text{NiO}_3$	4.1662	8.4015	2.0166	0.1962
$\text{CsYb}_2\text{NiO}_3$	3.9943	6.8090	1.7047	0.1853

TABLE V. Structural parameters of the studied G-type  $A_2\text{NiO}_2B'_2$  and  $A'_2\text{NiO}_2B_2$  nickelates ( $I4/mmm$ ) obtained with PBEsol functional. The  $A$  ( $A'$ ) atoms occupy the 4e site  $(0,0,\pm z)$ , and Ni atoms, O atoms in the  $\text{NiO}_2$  layer, and  $B'$  ( $B$ ) atoms in the  $AB'_2$  ( $A'B_2$ ) layer are located at the 2a, 4c, and 4d sites, respectively. Dynamically stable compositions are shown in bold.

Composition	$a$ (Å)	$c$ (Å)	$c/a$	$z$
$\text{Y}_2\text{NiO}_2B'_2$	3.7913	11.5016	3.0336	0.3615
<b><math>\text{La}_2\text{NiO}_2B'_2</math></b>	3.9289	12.4049	3.1573	0.3637
<b><math>\text{Nd}_2\text{NiO}_2B'_2</math></b>	3.8731	12.0737	3.1173	0.3627
$\text{Lu}_2\text{NiO}_2B'_2$	3.7578	11.2515	2.9942	0.3613
<b><math>A'_2\text{NiO}_2\text{F}_2</math></b>	3.9928	13.3419	3.3415	0.3725
$A'_2\text{NiO}_2\text{Cl}_2$	4.2286	14.8511	3.5121	0.3898
$A'_2\text{NiO}_2\text{Br}_2$	4.3500	15.2682	3.5099	0.3944
$A'_2\text{NiO}_2\text{I}_2$	4.4956	16.2578	3.6164	0.4042

TABLE VI. Structural parameters of the studied  $\text{H}_2$ -type  $A'_2\text{NiO}_2B_2$  nickelates ( $I4/mmm$ ) obtained with PBEsol functional. The  $A'$  and  $B$  atoms occupy the 4e site  $(0,0,\pm z)$ , and Ni atoms and O atoms are located at the 2a and 4c sites, respectively. Dynamically stable compositions are shown in bold.

Composition	$a$ (Å)	$c$ (Å)	$c/a$	$z_{A'}$	$z_B$
$A'_2\text{NiO}_2\text{F}_2$	3.8709	14.1021	3.6431	0.3787	0.1998
<b><math>A'_2\text{NiO}_2\text{Cl}_2</math></b>	3.9749	16.1162	4.0546	0.3953	0.1911
<b><math>A'_2\text{NiO}_2\text{Br}_2</math></b>	3.9884	17.7762	4.4570	0.4053	0.1848
<b><math>A'_2\text{NiO}_2\text{I}_2</math></b>	4.0113	20.8415	5.1957	0.4196	0.1735

TABLE VII. Structural parameters of the 1214-family  $AB_2\text{PdO}_4$  structures ( $P4/mmm$ ) optimized with PBEsol. The fractional coordinates of each atom are as follows:  $A:(0,0,\frac{1}{2})$ ,  $B:(\frac{1}{2},\frac{1}{2},\pm z)$ ,  $\text{Pd}:(0,0,0)$ ,  $\text{O}:(0,\frac{1}{2},0)$ ,  $(\frac{1}{2},0,0)$ ,  $(\frac{1}{2},0,\frac{1}{2})$ ,  $(0,\frac{1}{2},\frac{1}{2})$ . All compositions are dynamically unstable.

Composition	$a$ (Å)	$c$ (Å)	$c/a$	$z$
$\text{LiSc}_2\text{PdO}_4$	3.8422	5.6742	1.4768	0.2669
$\text{LiY}_2\text{PdO}_4$	3.9393	6.0890	1.5457	0.2616
$\text{LiNd}_2\text{PdO}_4$	4.0064	6.3708	1.5902	0.2604
$\text{LiLa}_2\text{PdO}_4$	4.0482	6.4982	1.6052	0.2598
$\text{NaSc}_2\text{PdO}_4$	3.9669	5.7111	1.4397	0.2652
$\text{NaY}_2\text{PdO}_4$	4.0567	6.0885	1.5009	0.2601
$\text{NaNd}_2\text{PdO}_4$	4.1199	6.3370	1.5382	0.2589
$\text{NaLa}_2\text{PdO}_4$	4.1603	6.4499	1.5503	0.2582
$\text{KSc}_2\text{PdO}_4$	4.1886	5.7432	1.3711	0.2570
$\text{KY}_2\text{PdO}_4$	4.2669	6.1080	1.4315	0.2560
$\text{KNd}_2\text{PdO}_4$	4.3198	6.3158	1.4621	0.2554
$\text{KLa}_2\text{PdO}_4$	4.3549	6.4244	1.4752	0.2561
$\text{RbSc}_2\text{PdO}_4$	4.2834	5.7581	1.3443	0.2443
$\text{RbY}_2\text{PdO}_4$	4.3665	6.0847	1.3935	0.2477
$\text{RbNd}_2\text{PdO}_4$	4.4161	6.2783	1.4217	0.2477
$\text{RbLa}_2\text{PdO}_4$	4.4491	6.4089	1.4405	0.2483
$\text{CsSc}_2\text{PdO}_4$	4.3891	5.8343	1.3293	0.2310
$\text{CsY}_2\text{PdO}_4$	4.4666	6.0926	1.3641	0.2384
$\text{CsNd}_2\text{PdO}_4$	4.5077	6.2677	1.3904	0.2394
$\text{CsLa}_2\text{PdO}_4$	4.5325	6.4134	1.4150	0.2386

TABLE VIII. Structural parameters of the 1213-family  $AB_2\text{PdO}_3$  structures ( $P4/mmm$ ) optimized with PBEsol. The fractional coordinates of each atom are as follows:  $A:(0,0,\frac{1}{2})$ ,  $B:(\frac{1}{2},\frac{1}{2},\pm z)$ , Pd:  $(0,0,0)$ , O:  $(0,\frac{1}{2},0)$ ,  $(\frac{1}{2},0,0)$ ,  $(\frac{1}{2},\frac{1}{2},\frac{1}{2})$ . Dynamically stable compositions are shown in bold.

Composition	$a$ (Å)	$c$ (Å)	$c/a$	$z$
LiMg <sub>2</sub> PdO <sub>3</sub>	3.9993	6.2141	1.5538	0.2020
LiCa <sub>2</sub> PdO <sub>3</sub>	4.0825	6.9881	1.7117	0.1973
LiSr <sub>2</sub> PdO <sub>3</sub>	4.1412	7.6276	1.8419	0.1983
LiBa <sub>2</sub> PdO <sub>3</sub>	4.1826	8.3593	1.9986	0.2021
LiYb <sub>2</sub> PdO <sub>3</sub>	4.0450	6.7165	1.6604	0.1892
NaMg <sub>2</sub> PdO <sub>3</sub>	4.0256	6.2507	1.5528	0.2017
NaCa <sub>2</sub> PdO <sub>3</sub>	4.1102	6.9907	1.7008	0.1961
NaSr <sub>2</sub> PdO <sub>3</sub>	4.1717	7.6125	1.8248	0.1968
NaBa <sub>2</sub> PdO <sub>3</sub>	4.2202	8.3234	1.9723	0.2003
NaYb <sub>2</sub> PdO <sub>3</sub>	4.0679	6.7281	1.6540	0.1886
KMg <sub>2</sub> PdO <sub>3</sub>	4.0811	6.2876	1.5407	0.2004
KCa <sub>2</sub> PdO <sub>3</sub>	4.1690	6.9745	1.6729	0.1932
<b>KSr<sub>2</sub>PdO<sub>3</sub></b>	4.2324	7.5722	1.7891	0.1937
KBa <sub>2</sub> PdO <sub>3</sub>	4.2901	8.2544	1.9241	0.1966
KYb <sub>2</sub> PdO <sub>3</sub>	4.1168	6.7316	1.6352	0.1866
RbMg <sub>2</sub> PdO <sub>3</sub>	4.1151	6.3123	1.5340	0.2001
RbCa <sub>2</sub> PdO <sub>3</sub>	4.1987	6.9768	1.6616	0.1926
<b>RbSr<sub>2</sub>PdO<sub>3</sub></b>	4.2611	7.5613	1.7745	0.1929
RbBa <sub>2</sub> PdO <sub>3</sub>	4.3210	8.2297	1.9046	0.1958
RbYb <sub>2</sub> PdO <sub>3</sub>	4.1437	6.7382	1.6261	0.1863
CsMg <sub>2</sub> PdO <sub>3</sub>	4.1709	6.3377	1.5195	0.1997
CsCa <sub>2</sub> PdO <sub>3</sub>	4.2439	6.9808	1.6449	0.1919
<b>CsSr<sub>2</sub>PdO<sub>3</sub></b>	4.3015	7.5537	1.7561	0.1920
<b>CsBa<sub>2</sub>PdO<sub>3</sub></b>	4.3609	8.2095	1.8825	0.1948
CsYb <sub>2</sub> PdO <sub>3</sub>	4.1859	6.7456	1.6115	0.1859

TABLE X. Structural parameters of the studied H<sub>2</sub>-type  $A'_2\text{PdO}_2B_2$  palladates ( $I4/mmm$ ) obtained with PBEsol functional. The  $A'$  and  $B$  atoms occupy the 4e site  $(0,0,\pm z)$ , and Ni atoms and O atoms are located at the 2a and 4c sites, respectively. All compositions are dynamically unstable.

Composition	$a$ (Å)	$c$ (Å)	$c/a$	$z_{A'}$	$z_B$
$A'_2\text{PdO}_2\text{F}_2$	4.1337	13.8978	3.3621	0.3807	0.2077
$A'_2\text{PdO}_2\text{Cl}_2$	4.1773	15.6770	3.7529	0.3937	0.1946
$A'_2\text{PdO}_2\text{Br}_2$	4.2058	16.5014	3.9235	0.3994	0.1919
$A'_2\text{PdO}_2\text{I}_2$	4.2102	19.4025	4.6085	0.4148	0.1790

TABLE IX. Structural parameters of the studied G-type  $A_2\text{NiO}_2B'_2$  and  $A'_2\text{NiO}_2B_2$  palladates ( $I4/mmm$ ) obtained with PBEsol functional. The  $A$  ( $A'$ ) atoms occupy the 4e site  $(0,0,\pm z)$ , and Pd atoms, O atoms in the PdO<sub>2</sub> layer, and  $B'$  ( $B$ ) atoms in the  $AB'_2$  ( $A'B_2$ ) layer are located at the 2a, 4c, and 4d sites, respectively. Dynamically stable compositions are shown in bold.

Composition	$a$ (Å)	$c$ (Å)	$c/a$	$z$
Y <sub>2</sub> PdO <sub>2</sub> B' <sub>2</sub>	3.9846	11.2469	2.8226	0.3572
La <sub>2</sub> PdO <sub>2</sub> B' <sub>2</sub>	4.1027	12.0643	2.9406	0.3610
Nd <sub>2</sub> PdO <sub>2</sub> B' <sub>2</sub>	4.0530	11.7608	2.9017	0.3593
Lu <sub>2</sub> PdO <sub>2</sub> B' <sub>2</sub>	3.9594	10.9881	2.7752	0.3568
<b><math>A'_2\text{PdO}_2\text{F}_2</math></b>	4.1914	12.8875	3.0747	0.3706
<b><math>A'_2\text{PdO}_2\text{Cl}_2</math></b>	4.3623	14.6197	3.3514	0.3891
$A'_2\text{PdO}_2\text{Br}_2$	4.4572	15.1064	3.3892	0.3938
$A'_2\text{PdO}_2\text{I}_2$	4.6123	15.9378	3.4555	0.4020

TABLE XI. Energy of the interstitial  $s$  orbital and the cation  $d_{xy}$  orbital in the Ni-based compounds.  $E_s$  and  $E_{d_{xy}}$  are the onsite potentials of the  $s$  and  $d_{xy}$  Wannier orbitals, respectively.  $E_b^k$  and  $E_a^k$  are the energy levels of the bonding and antibonding states between the  $s$  and  $d_{xy}$  orbitals at the  $k$  point, respectively.  $\Delta E_{sd}$  is the energy difference between the  $s$  and  $d_{xy}$  states,  $\Delta E_{sd} = E_s - E_{d_{xy}}$ .  $\bar{E}_{sd}$  is the average of  $E_s$  and  $E_{d_{xy}}$ .  $\Delta E_{ba}^k$  is the energy difference between the bonding and antibonding bands at the  $k$  point. The unit for length is Å. The energy is measured with respect to the Fermi level in units of eV.

	$a$	$c$	$E_s$	$E_{d_{xy}}$	$E_b^A$	$E_a^A$			$\Delta E_{sd}$	$\bar{E}_{sd}$	$\Delta E_{ba}^A$	
LaNiO <sub>2</sub>	3.959	3.375	4.024	3.080	-1.584	9.625			0.944	3.552	11.209	
NdNiO <sub>2</sub>	3.921	3.281	4.017	3.046	-1.567	9.270			0.971	3.532	10.837	
	$a$	$c$	$E_s$	$E_{d_{xy}}$	$E_b^M$	$E_a^M$	$E_b^A$	$E_a^A$	$\Delta E_{sd}$	$\bar{E}_{sd}$	$\Delta E_{ba}^M$	$\Delta E_{ba}^A$
LiLa <sub>2</sub> NiO <sub>4</sub>	3.904	6.583	4.471	3.532	-1.121	10.328	0.675	10.298	0.939	4.002	11.449	9.623
LiNd <sub>2</sub> NiO <sub>4</sub>	3.858	6.440	4.514	3.435	-1.141	9.832	0.724	9.957	1.079	3.975	10.973	9.233
KCa <sub>2</sub> NiO <sub>3</sub>	3.937	7.109	3.932	4.197	0.549	8.069	-0.109	6.658	-0.265	4.065	7.520	6.767
KSr <sub>2</sub> NiO <sub>3</sub>	4.005	7.756	4.388	4.787	0.247	10.270	-0.272	10.796	-0.399	4.588	10.023	11.068
KBa <sub>2</sub> NiO <sub>3</sub>	4.037	8.514	4.825	4.108	-0.345	11.407	-0.688	11.355	0.717	4.467	11.752	12.043
KYb <sub>2</sub> NiO <sub>3</sub>	3.890	6.839	5.037	5.415	0.026	10.609	-0.722	11.709	-0.378	5.226	10.583	12.431
RbCa <sub>2</sub> NiO <sub>3</sub>	3.983	7.091	4.221	3.895	0.917	7.897	0.009	6.776	0.326	4.058	6.980	6.767
RbSr <sub>2</sub> NiO <sub>3</sub>	4.051	7.724	4.307	4.740	0.559	10.043	-0.191	11.066	-0.433	4.524	9.484	11.257
RbBa <sub>2</sub> NiO <sub>3</sub>	4.093	8.460	4.607	4.059	-0.076	11.180	-0.603	11.451	0.548	4.333	11.256	12.054
RbYb <sub>2</sub> NiO <sub>3</sub>	3.933	6.824	4.851	5.345	0.430	10.225	-0.653	12.443	-0.494	5.098	9.795	13.096
	$a$	$c$	$E_s$	$E_{d_{xy}}$	$E_b^X$	$E_a^X$	$E_b^P$	$E_a^P$	$\Delta E_{sd}$	$\bar{E}_{sd}$	$\Delta E_{ba}^X$	$\Delta E_{ba}^P$
La <sub>2</sub> NiO <sub>2</sub> B <sub>2</sub> ' (G)	3.929	12.405	4.688	3.143	-0.121	9.768	-0.114	9.772	1.545	3.916	9.889	9.886
Nd <sub>2</sub> NiO <sub>2</sub> B <sub>2</sub> ' (G)	3.873	12.074	4.524	2.965	-0.209	9.440	-0.204	9.467	1.559	3.745	9.649	9.671
A <sub>2</sub> 'NiO <sub>2</sub> F <sub>2</sub> (G)	3.993	13.342	4.785	3.795	-0.301	11.312	-0.295	11.381	0.990	4.290	11.613	11.676
A <sub>2</sub> 'NiO <sub>2</sub> Cl <sub>2</sub> (H <sub>2</sub> )	3.975	16.116	5.399	3.504	1.002	8.754	0.979	8.671	1.895	4.452	7.752	7.692
A <sub>2</sub> 'NiO <sub>2</sub> Br <sub>2</sub> (H <sub>2</sub> )	3.988	17.776	5.280	3.530	0.898	9.033	0.874	9.004	1.750	4.405	8.135	8.130
A <sub>2</sub> 'NiO <sub>2</sub> I <sub>2</sub> (H <sub>2</sub> )	4.011	20.842	5.126	3.698	0.973	9.472	0.960	9.269	1.428	4.412	8.499	8.309

TABLE XII. Energy of the interstitial  $s$  orbital and the cation  $d_{xy}$  orbital in the Pd-based compounds.  $E_s$  and  $E_{d_{xy}}$  are the onsite potentials of the  $s$  and  $d_{xy}$  Wannier orbitals, respectively.  $E_b^k$  and  $E_a^k$  are the energy levels of the bonding and antibonding states between the  $s$  and  $d_{xy}$  orbitals at the  $k$  point, respectively.  $\Delta E_{sd}$  is the energy difference between the  $s$  and  $d_{xy}$  states,  $\Delta E_{sd} = E_s - E_{d_{xy}}$ .  $\bar{E}_{sd}$  is the average of  $E_s$  and  $E_{d_{xy}}$ .  $\Delta E_{ba}^k$  is the energy difference between bonding and antibonding bands at the  $k$  point. The unit for length is Å. The energy is measured with respect to the Fermi level in units of eV.

	$a$	$c$	$E_s$	$E_{d_{xy}}$	$E_b^M$	$E_a^M$	$E_b^A$	$E_a^A$	$\Delta E_{sd}$	$\bar{E}_{sd}$	$\Delta E_{ba}^M$	$\Delta E_{ba}^A$
KSr <sub>2</sub> PdO <sub>3</sub>	4.232	7.572	5.002	4.854	0.744	9.517	0.102	10.586	0.148	4.928	8.773	10.484
RbSr <sub>2</sub> PdO <sub>3</sub>	4.261	7.561	4.302	4.736	1.070	9.531	0.191	11.041	-0.434	4.519	8.461	10.850
CsSr <sub>2</sub> PdO <sub>3</sub>	4.302	7.554	4.359	4.667	1.565	9.139	0.312	11.114	-0.308	4.513	7.574	10.802
CsBa <sub>2</sub> PdO <sub>3</sub>	4.361	8.210	4.178	4.266	0.746	9.427	-0.196	10.910	-0.088	4.222	8.681	11.106
	$a$	$c$	$E_s$	$E_{d_{xy}}$	$E_b^X$	$E_a^X$	$E_b^P$	$E_a^P$	$\Delta E_{sd}$	$\bar{E}_{sd}$	$\Delta E_{ba}^X$	$\Delta E_{ba}^P$
A <sub>2</sub> 'PdO <sub>2</sub> F <sub>2</sub> (G)	4.191	12.888	4.772	3.271	-0.163	9.860	-0.167	9.750	1.501	4.022	10.023	9.917
A <sub>2</sub> 'PdO <sub>2</sub> Cl <sub>2</sub> (G)	4.362	14.620	4.836	3.679	0.552	9.709	0.535	9.342	1.157	4.258	9.157	8.807



- [1] D. Li, K. Lee, B. Y. Wang, M. Osada, S. Crossley, H. R. Lee, Y. Cui, Y. Hikita, and H. Y. Hwang, Superconductivity in an infinite-layer nickelate, *Nature* **572**, 624 (2019).
- [2] A. S. Botana and M. R. Norman, arXiv:1908.10946.
- [3] H. Sakakibara, H. Usui, K. Suzuki, T. Kotani, H. Aoki, and K. Kuroki, arXiv:1909.00060.
- [4] J. Hirsch and F. Marsiglio, Hole superconductivity in infinite-layer nickelates, *Physica C: Superconductivity and its Applications* **566**, 1353534 (2019).
- [5] K. Yamagami, K. Ishii, Y. Hirata, K. Ikeda, J. Miyawaki, Y. Harada, M. Miyazaki, S. Asano, M. Fujita, and H. Wadati, Localized Charge Excitations of  $\text{La}_{2-x}\text{Sr}_x\text{NiO}_{4+\delta}$  Revealed by Oxygen  $K$ -edge Resonant Inelastic X-ray Scattering, arXiv:1909.01942.
- [6] M. Hepting, D. Li, C. J. Jia, H. Lu, E. Paris, Y. Tseng, X. Feng, M. Osada, E. Been, Y. Hikita, Y. D. Chuang, Z. Hussain, K. J. Zhou, A. Nag, M. Garcia-Fernandez, M. Rossi, H. Y. Huang, D. J. Huang, Z. X. Shen, T. Schmitt, H. Y. Hwang, B. Moritz, J. Zaanen, T. P. Devereaux, and W. S. Lee, Electronic structure of the parent compound of superconducting infinite-layer nickelates, arXiv:1909.02678.
- [7] X. Wu, D. D. Sante, T. Schwemmer, W. Hanke, H. Y. Hwang, S. Raghu, and R. Thomale, Robust  $d_{x^2-y^2}$ -wave superconductivity of infinite-layer nickelates, arXiv:1909.03015.
- [8] Y. Nomura, M. Hirayama, T. Tadano, Y. Yoshimoto, K. Nakamura, and R. Arita, Formation of 2D single-component correlated electron system and band engineering in the nickelate superconductor  $\text{NdNiO}_2$ , arXiv:1909.03942.
- [9] J. Gao, Z. Wang, C. Fang, and H. Weng, Electronic structures and topological properties in nickelates  $\text{Ln}_{n+1}\text{Ni}_n\text{O}_{2n+2}$ , arXiv:1909.04657.
- [10] H. Zhang, L. Jin, S. Wang, B. Xi, X. Shi, F. Ye, and J.-W. Mei, Effective Hamiltonian for superconducting Ni oxides  $\text{Nd}_{1-x}\text{Sr}_x\text{NiO}_2$ , (), arXiv:1909.07427.
- [11] N. Singh, A “road-map” of Nickelate superconductivity, arXiv:1909.07688.
- [12] G.-M. Zhang, Y.-F. Yang, and F.-C. Zhang, Self-doped Mott insulator for parent compounds of nickelate superconductors (), arXiv:1909.11845.
- [13] Y.-H. Zhang and A. Vishwanath, Kondo resonance and  $d$ -wave superconductivity in the  $t - J$  model with spin one holes: possible applications to the nickelate superconductor  $\text{Nd}_{1-x}\text{Sr}_x\text{NiO}_2$ , arXiv:1909.12865.
- [14] P. Jiang, L. Si, Z. Liao, and Z. Zhong, Electronic structure of rare-earth infinite-layer  $\text{ReNiO}_2$  ( $\text{Re}=\text{La}, \text{Nd}$ ), arXiv:1909.13634.
- [15] P. Werner and S. Hoshino, Nickelate superconductors — Multiorbital nature and spin freezing, arXiv:1910.00473.
- [16] L.-H. Hu and C. Wu, Two-band model for magnetism and superconductivity in nickelates, arXiv:1910.02482.
- [17] J. G. Bednorz and K. A. Müller, Possible high  $T_c$  superconductivity in the Ba-La-Cu-O system, *Zeitschrift für Physik B Condensed Matter* **64**, 189 (1986).
- [18] Y. Kamihara, T. Watanabe, M. Hirano, and H. Hosono, Iron-based layered superconductor  $\text{La}[\text{o}1\text{-xfx}]\text{FeAs}$  ( $x = 0.05\text{--}0.12$ ) with  $t_c = 26$  K, *J. Am. Chem. Soc.* **130**, 3296 (2008), pMID: 18293989.
- [19] Y. Mizuguchi, H. Fujihisa, Y. Gotoh, K. Suzuki, H. Usui, K. Kuroki, S. Demura, Y. Takano, H. Izawa, and O. Miura,  $\text{BiS}_2$ -based layered superconductor  $\text{Bi}_4\text{O}_4\text{S}_3$ , *Phys. Rev. B* **86**, 220510 (2012).
- [20] K.-W. Lee and W. E. Pickett, Infinite-layer  $\text{LaNiO}_2$ :  $\text{Ni}^{1+}$  is not  $\text{Cu}^{2+}$ , *Phys. Rev. B* **70**, 165109 (2004).
- [21] Y. Tokura and T. Arima, New classification method for layered copper oxide compounds and its application to design of new high  $T_c$  superconductors, *Jpn. J. Appl. Phys.* **29**, 2388 (1990).
- [22] T. Ozaki, Variationally optimized atomic orbitals for large-scale electronic structures, *Phys. Rev. B* **67**, 155108 (2003).
- [23] M. A. Hayward, M. A. Green, M. J. Rosseinsky, and J. Sloan, Sodium Hydride as a Powerful Reducing Agent for Topotactic Oxide Deintercalation: Synthesis and Characterization of the Nickel(I) Oxide  $\text{LaNiO}_2$ , *J. Am. Chem. Soc.* **121**, 8843 (1999).
- [24] M. Hayward and M. Rosseinsky, Synthesis of the infinite layer  $\text{Ni}(\text{I})$  phase  $\text{NdNiO}_{2+x}$  by low temperature reduction of  $\text{NdNiO}_3$  with sodium hydride, *Solid State Sci.* **5**, 839 (2003), international Conference on Inorganic Materials 2002.
- [25] M. Crespin, O. Isnard, F. Dubois, J. Choisnet, and P. Odier,  $\text{LaNiO}_2$ : Synthesis and structural characterization, *J. Solid State Chem.* **178**, 1326 (2005).
- [26] M. Kawai, S. Inoue, M. Mizumaki, N. Kawamura, N. Ichikawa, and Y. Shimakawa, Reversible changes of epitaxial thin films from perovskite  $\text{LaNiO}_3$  to infinite-layer structure  $\text{LaNiO}_2$ , *Appl. Phys. Lett.* **94**, 082102 (2009).
- [27] A. Boehlke and H. Mller-Buschbaum,  $\text{Ba}_2\text{CuO}_2\text{I}$ : Eine Verbindung mit neuem Strukturtyp und ein Beitrag zur  $\text{Ba}_2\text{CuO}_2\text{Br}$  mit  $\text{Ba}_2\text{CuO}_2\text{Cl}$ -Struktur (1990).
- [28] Y. Tokura, H. Takagi, and S. Uchida, A superconducting copper oxide compound with electrons as the charge carriers, *Nature* **337**, 345 (1989).
- [29] P. Lacorre, Passage from  $t$ -type to  $t'$ -type arrangement by reducing  $\text{r}_4\text{Ni}_3\text{O}_{10}$  to  $\text{r}_4\text{Ni}_3\text{O}_8$  ( $\text{r} = \text{La}, \text{Pr}, \text{Nd}$ ), *J. Solid State Chem.* **97**, 495 (1992).
- [30] R. Retoux, J. Rodriguez-Carvajal, and P. Lacorre, Neutron diffraction and TEM studies of the crystal structure and defects of  $\text{Nd}_4\text{Ni}_3\text{O}_8$ , *J. Solid State Chem.* **140**, 307 (1998).
- [31] V. V. Poltavets, K. A. Lokshin, M. Croft, T. K. Mandal, T. Egami, and M. Greenblatt, Crystal structures of  $\text{Ln}_4\text{Ni}_3\text{O}_8$  ( $\text{Ln} = \text{La}, \text{Nd}$ ) triple layer  $t'$ -type nickelates, *Inorg. Chem.* **46**, 10887 (2007).
- [32] V. V. Poltavets, K. A. Lokshin, S. Dikmen, M. Croft, T. Egami, and M. Greenblatt,  $\text{La}_3\text{Ni}_2\text{O}_6$ : A new double  $t'$ -type nickelate with infinite  $\text{Ni}^{1+}/2+\text{o}2$  layers, *J. Am. Chem. Soc.* **128**, 9050 (2006).
- [33] J. L. Kissick, C. Greaves, P. P. Edwards, V. M. Cherkashenko, E. Z. Kurmaev, S. Bartkowski, and M. Neumann, Synthesis, structure, and XPS characterization of the stoichiometric phase  $\text{Sr}_2\text{CuO}_2\text{F}_2$ , *Phys. Rev. B* **56**, 2831 (1997).
- [34] T. Baikié, E. L. Dixon, J. F. Rooms, N. A. Young, and M. G. Francesconi,  $\text{Ba}_{2-x}\text{Sr}_x\text{PdO}_2\text{F}_2$  ( $0 \leq x \leq 1.5$ ): The first palladium-oxide-fluorides, *Chem. Commun.*, 1580 (2003).

- [35] L. L. Miller, X. L. Wang, S. X. Wang, C. Stassis, D. C. Johnston, J. Faber, and C.-K. Loong, Synthesis, structure, and properties of  $\text{Sr}_2\text{CuO}_2\text{Cl}_2$ , *Phys. Rev. B* **41**, 1921 (1990).
- [36] Z. Hiroi, N. Kobayashi, and M. Takano, Probable hole-doped superconductivity without apical oxygens in  $(\text{Ca},\text{Na})_2\text{CuO}_2\text{Cl}_2$ , *Nature* **371**, 139 (1994).
- [37] Y. Tsujimoto, C. I. Sathish, Y. Matsushita, K. Yamaura, and T. Uchikoshi, New members of layered oxychloride perovskites with square planar coordination:  $\text{Sr}_2\text{MO}_2\text{Cl}_2$  ( $M = \text{Mn}, \text{Ni}$ ) and  $\text{Ba}_2\text{PdO}_2\text{Cl}_2$ , *Chem. Commun.* **50**, 5915 (2014).
- [38] W. Sun, S. T. Dacek, S. P. Ong, G. Hautier, A. Jain, W. D. Richards, A. C. Gamst, K. A. Persson, and G. Ceder, The thermodynamic scale of inorganic crystalline metastability, *Sci. Adv.* **2**, 10.1126/sciadv.1600225 (2016).
- [39] J. Zaanen, G. A. Sawatzky, and J. W. Allen, Band gaps and electronic structure of transition-metal compounds, *Phys. Rev. Lett.* **55**, 418 (1985).
- [40] N. Marzari and D. Vanderbilt, Maximally localized generalized wannier functions for composite energy bands, *Phys. Rev. B* **56**, 12847 (1997).
- [41] I. Souza, N. Marzari, and D. Vanderbilt, Maximally localized wannier functions for entangled energy bands, *Phys. Rev. B* **65**, 035109 (2001).
- [42] F. Aryasetiawan, M. Imada, A. Georges, G. Kotliar, S. Biermann, and A. I. Lichtenstein, Frequency-dependent local interactions and low-energy effective models from electronic structure calculations, *Phys. Rev. B* **70**, 195104 (2004).
- [43] T. Tadano, Y. Nomura, and M. Imada, Ab initio derivation of an effective Hamiltonian for the  $\text{La}_2\text{CuO}_4/\text{La}_{1.55}\text{Sr}_{0.45}\text{CuO}_4$  heterostructure, *Phys. Rev. B* **99**, 155148 (2019).
- [44] M. Hirayama, Y. Yamaji, T. Misawa, and M. Imada, Ab initio effective Hamiltonians for cuprate superconductors, *Phys. Rev. B* **98**, 134501 (2018).
- [45] M. Hirayama, T. Misawa, T. Ohgoe, Y. Yamaji, and M. Imada, Effective Hamiltonian for cuprate superconductors derived from multiscale ab initio scheme with level renormalization, *Phys. Rev. B* **99**, 245155 (2019).
- [46] P. Werner, R. Sakuma, F. Nilsson, and F. Aryasetiawan, Dynamical screening in  $\text{La}_2\text{CuO}_4$ , *Phys. Rev. B* **91**, 125142 (2015).
- [47] S. W. Jang, H. Sakakibara, H. Kino, T. Kotani, K. Kuroki, and M. J. Han, Direct theoretical evidence for weaker correlations in electron-doped and Hg-based hole-doped cuprates, *Sci. Rep.* **6**, 33397 EP (2016).
- [48] F. Nilsson, K. Karlsson, and F. Aryasetiawan, Dynamically screened Coulomb interaction in the parent compounds of hole-doped cuprates: Trends and exceptions, *Phys. Rev. B* **99**, 075135 (2019).
- [49] E. Pavarini, I. Dasgupta, T. Saha-Dasgupta, O. Jepsen, and O. K. Andersen, Band-Structure Trend in Hole-Doped Cuprates and Correlation with  $T_{\text{cmax}}$ , *Phys. Rev. Lett.* **87**, 047003 (2001).
- [50] K. Momma and F. Izumi, *VESTA3* for three-dimensional visualization of crystal, volumetric and morphology data, *J. Appl. Crystallogr.* **44**, 1272 (2011).
- [51] G. Kresse and J. Furthmüller, Efficient iterative schemes for ab initio total-energy calculations using a plane-wave basis set, *Phys. Rev. B* **54**, 11169 (1996).
- [52] P. E. Blöchl, Projector augmented-wave method, *Phys. Rev. B* **50**, 17953 (1994).
- [53] G. Kresse and D. Joubert, From ultrasoft pseudopotentials to the projector augmented-wave method, *Phys. Rev. B* **59**, 1758 (1999).
- [54] P. Giannozzi, O. Andreussi, T. Brumme, O. Bunau, M. B. Nardelli, M. Calandra, R. Car, C. Cavazzoni, D. Ceresoli, M. Cococcioni, N. Colonna, I. Carnimeo, A. D. Corso, S. de Gironcoli, P. Delugas, R. A. D. Jr, A. Ferretti, A. Floris, G. Fratesi, G. Fugallo, R. Gebauer, U. Gerstmann, F. Giustino, T. Gorni, J. Jia, M. Kawamura, H.-Y. Ko, A. Kokalj, E. Kkbenli, M. Lazzeri, M. Marsili, N. Marzari, F. Mauri, N. L. Nguyen, H.-V. Nguyen, A. O. de-la Roza, L. Paulatto, S. Ponc, D. Rocca, R. Sabatini, B. Santra, M. Schlipf, A. P. Seitsonen, A. Smogunov, I. Timrov, T. Thonhauser, P. Umari, N. Vast, X. Wu, and S. Baroni, Advanced capabilities for materials modelling with QUANTUM ESPRESSO, *J. Phys. Condens. Matter* **29**, 465901 (2017).
- [55] D. R. Hamann, Optimized norm-conserving vanderbilt pseudopotentials, *Phys. Rev. B* **88**, 085117 (2013).
- [56] M. van Setten, M. Giantomassi, E. Bousquet, M. Verstraete, D. Hamann, X. Gonze, and G.-M. Rignanese, The PseudoDojo: Training and grading a 85 element optimized norm-conserving pseudopotential table, *Comput. Phys. Commun.* **226**, 39 (2018).
- [57] J. P. Perdew, A. Ruzsinszky, G. I. Csonka, O. A. Vydrov, G. E. Scuseria, L. A. Constantin, X. Zhou, and K. Burke, Restoring the density-gradient expansion for exchange in solids and surfaces, *Phys. Rev. Lett.* **100**, 136406 (2008).
- [58] R. Wahl, D. Vogtenhuber, and G. Kresse,  $\text{srTiO}_3$  and  $\text{BaTiO}_3$  revisited using the projector augmented wave method: Performance of hybrid and semilocal functionals, *Phys. Rev. B* **78**, 104116 (2008).
- [59] G. I. Csonka, J. P. Perdew, A. Ruzsinszky, P. H. T. Philipsen, S. Lebègue, J. Paier, O. A. Vydrov, and J. G. Ángyán, Assessing the performance of recent density functionals for bulk solids, *Phys. Rev. B* **79**, 155107 (2009).
- [60] T. Tadano, Y. Gohda, and S. Tsuneyuki, Anharmonic force constants extracted from first-principles molecular dynamics: applications to heat transfer simulations, *J. Phys. Condens. Matter* **26**, 225402 (2014).
- [61] T. Tadano and S. Tsuneyuki, First-Principles Lattice Dynamics Method for Strongly Anharmonic Crystals, *J. Phys. Soc. Jpn.* **87**, 041015 (2018).
- [62] <https://sites.google.com/view/kazuma7k6r>.
- [63] Algorithms and applications of RESPACK can be found in Refs. [66–70].
- [64] J. P. Perdew, K. Burke, and M. Ernzerhof, Generalized Gradient Approximation Made Simple, *Phys. Rev. Lett.* **77**, 3865 (1996).
- [65] E. Şaşıoğlu, C. Friedrich, and S. Blügel, Effective coulomb interaction in transition metals from constrained random-phase approximation, *Phys. Rev. B* **83**, 121101 (2011).
- [66] K. Nakamura, Y. Nohara, Y. Yosimoto, and Y. Nomura, Ab initio *GW* plus cumulant calculation for isolated band systems: Application to organic conductor  $(\text{TMTSF})_2\text{PF}_6$  and transition-metal oxide  $\text{SrVO}_3$ , *Phys. Rev. B* **93**, 085124 (2016).
- [67] K. Nakamura, Y. Yoshimoto, T. Kosugi, R. Arita, and M. Imada, Ab initio Derivation of Low-Energy Model for  $\kappa$ -ET Type Organic Conductors, *J. Phys. Soc. Jpn.* **78**,

- 083710 (2009).
- [68] K. Nakamura, R. Arita, and M. Imada, Ab initio Derivation of Low-Energy Model for Iron-Based Superconductors LaFeAsO and LaFePO, *J. Phys. Soc. Jpn.* **77**, 093711 (2008).
- [69] Y. Nohara, S. Yamamoto, and T. Fujiwara, Electronic structure of perovskite-type transition metal oxides  $\text{LaMO}_3$  ( $M = \text{Ti} \sim \text{Cu}$ ) by  $U + \text{GW}$  approximation, *Phys. Rev. B* **79**, 195110 (2009).
- [70] T. Fujiwara, S. Yamamoto, and Y. Ishii, Generalization of the Iterative Perturbation Theory and Metal–Insulator Transition in Multi-Orbital Hubbard Bands, *J. Phys. Soc. Jpn.* **72**, 777 (2003).